AIMS Mathematics, 10(10): 23261–23291.
DOI: 10.3934/math.20251032
Received: 19 March 2025
Revised: 01 August 2025
Accepted: 21 August 2025
Published: 14 October 2025

http://www.aimspress.com/journal/Math

Research article

Deep neural network applications in mathematical epidemiology: Case of rabies virus

Mutum Zico Meetei[1], Ramsha Shafqat[2,*], Ahmed H. Msmali[1] and Waleed Hamali[1]

[1] Department of Mathematics, College of Science, Jazan University, P.O. Box 114, Jazan 45142, Saudi Arabia

[2] Department of Mathematics and Statistics, The University of Lahore, Sargodha 40100, Pakistan

* **Correspondence:** Email: ramshawarriach@gmail.com.

Abstract: This research uses Susceptible–Exposed–Infectious–Recovered (SEIR) and Susceptible–Exposed–Infectious–Vaccinated (SEIV) models to analyze rabies transmission in human and canine populations. The framework includes eight epidemiological compartments to evaluate intervention strategies. A fractional-order model is employed using the Atangana-Baleanu derivative in the Caputo sense to capture memory and the system's complexity. The model's validity is established through qualitative analysis. Existence and uniqueness are confirmed via fixed-point theory, and Ulam-Hyers criteria assess robustness. Numerical solutions are obtained using the iterative Adams and Adams-Bashforth methods for accurate time-series simulations. Numerical experiments evaluate vaccination effects under a constant rate for a subset of the population. The results show that vaccination effectively reduces disease prevalence, emphasizing its critical role in rabies control. Deep neural network (DNN) techniques are applied for training, validation, and testing. The DNN has three hidden layers (10, 100, 10 neurons) and is trained over 1000 epochs using the Levenberg-Marquardt algorithm. The model achieves high predictive accuracy, with mean square errors as low as 0.00027 and root mean square errors under 0.17 across compartments. Overall, combining fractional calculus with deep learning provides a robust framework for modeling complex disease dynamics and offers valuable insights for public health strategies in regions with significant dog populations.

Keywords: rabies; mathematical modeling; fractional derivatives; dogs; qualitative analysis; Adam-Bashforth method; stability analysis; numerical simulation; ABC fractional derivative
Mathematics Subject Classification: 34D20, 34K20, 34K60, 92C60, 92D45

1. Introduction

Rabies is a viral infection caused by the *Lyssavirus* genus, leading to inflammation of the brain in mammals. It is primarily transmitted through bites or scratches from infected animals, with dogs serving as the main reservoir in endemic areas, accounting for over 99% of human cases [1, 2]. The disease incubation period varies widely, typically ranging from one to three months, but it can extend beyond a year, depending on the exposure site and viral load. Rabies is almost always fatal once clinical symptoms develop, underscoring the importance of vaccination and post-exposure prophylaxis [3].

Mathematical models based on the SEIR framework have been extensively used to study rabies transmission dynamics, and the effectiveness of interventions such as vaccination and culling [4–10]. These classical integer-order models describe the population as divided into susceptible, exposed, infected, and recovered compartments but do not account for the memory or hereditary properties inherent in disease progression.

Fractional calculus has emerged as a powerful tool to address these limitations by introducing derivatives of non-integer order, which inherently incorporate memory effects [11–13]. The Atangana-Baleanu-Caputo fractional derivative, in particular, features a non-singular kernel that enhances the model's accuracy and stability. Recent epidemiological studies have applied fractional differential equations to modeling infectious disease, demonstrating improved predictive capabilities and robustness compared to traditional models [14–16]. Recent studies have applied neural networks to fractional differential systems across various domains. For example, Anwar et al. [17] used stochastic adaptive networks with Grünwald-Letnikov differences for modeling coffee rust, while Raja et al. [18] developed predictive intelligent networks for a fractional tuberculosis-virus model. Similarly, Fida et al. [19] proposed a neuro-architecture-driven approach for fractional breast cancer risk analysis. These works highlight the growing interest in combining fractional calculus with artificial intelligence (AI) for complex systems, motivating our integration of the Atangana-Baleanu operator with deep neural networks (DNNs) for rabies dynamics.

While fractional models offer theoretical advantages, their application to modeling rabies remains limited. Concurrently, DNNs have gained prominence in epidemiology for their capacity to learn complex, nonlinear patterns from data [20–22]. DNNs have been successfully employed for forecasting, parameter estimation, and classification of infectious diseases.

Our study uniquely integrates fractional calculus with DNN techniques to model rabies transmission. We propose a fractional SEIR-SEIV model utilizing the Atangana-Baleanu-Caputo operator to capture memory effects in both human and dog populations and extend the dog compartments to include vaccination status. The DNN component approximates solutions to the fractional system, facilitating efficient computation and accurate prediction. Theoretical analysis ensures the existence, uniqueness, and stability of solutions, while numerical simulations demonstrate the impact of fractional order and vaccination on the dynamics of the disease.

This integrated framework advances rabies modeling by combining mechanistic and data-driven approaches, providing valuable insights for optimizing control strategies in endemic regions. Schematic diagram of the rabies transmission model integrating human and dog populations is shown in Figure 1. The manuscript is structured as follows: Section 2 covers essential definitions and concepts from fractional calculus. Section 3 discusses the theoretical findings, leveraging fixed-point theory and examining Ulam-Hyers stability under minor perturbations in the initial conditions.

Section 4 employs Adams-Bashforth methods to approximate the model's solutions, offering insights into its numerical behavior.

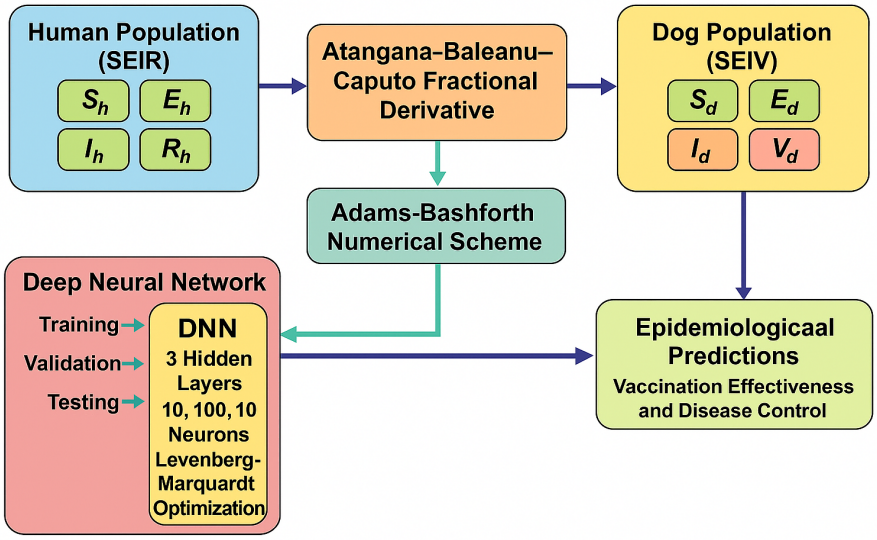

Figure 1. Schematic diagram of the rabies transmission model integrating human (SEIR) and dog (SEIV) populations.

2. Basic results

This section introduces essential notations and key definitions relevant to fractional calculus.

Definition 2.1. Let $\mathbf{U}(t)$ be a function such that $\xi \in [0, 1]$. The Caputo-type fractional derivative, represented as $\mathcal{ABC}$, is defined as:

$$^{\mathcal{ABC}}\mathbf{D}_t^{\xi}(\mathbf{U}(t)) = \frac{M(\xi)}{1-\xi}\int_0^t \mathbf{E}_{\xi}\left[\frac{-\xi}{1-\xi}(t-u)^{\xi}\right]\frac{d}{du}\mathbf{U}(u)\,du, \tag{2.1}$$

where $M(0) = M(1) = 1$ is the normalization function, and $\mathbf{E}_{\xi}$ denotes the Mittag-Leffler function, given by:

$$\mathbf{E}_{\xi}(y) = \sum_{k=0}^{\infty}\frac{y^k}{\Gamma(\xi k+1)}. \tag{2.2}$$

Definition 2.2. For a function $\mathbf{U}(t) \in L^1(0, T)$, the fractional integral in the $\mathcal{ABC}$ sense is given by

$$^{\mathcal{ABC}}\mathbf{I}_t^{\xi}\mathbf{U}(t) = \frac{1-\xi}{M(\xi)}\mathbf{U}(t) + \frac{\xi}{M(\xi)}\frac{1}{\Gamma(\xi)}\int_0^t (t-u)^{\xi-1}\mathbf{U}(u)\,du, \quad t > 0. \tag{2.3}$$

Lemma 2.1. *For $\xi \in (0, 1]$, the solution to the given fractional problem is expressed as*

$$\begin{aligned} ^{\mathcal{ABC}}\mathbf{D}_t^{\xi}\mathbf{U}(t) &= \mathbf{U}(t), \\ \mathbf{U}(t) &= \mathbf{U}_0 \end{aligned}$$

with the assumption

$$\mathbf{U}(t) = \mathbf{U}_0 + \frac{1-\xi}{M(\xi)}\mathbf{U}(t) + \frac{\xi}{M(\xi)}\frac{1}{\Gamma(\xi)}\int_0^t (t-u)^{\xi-1}\mathbf{U}(u)du. \tag{2.4}$$

Model formulation

In this study, we employ SEIR framework to model the human population and SEIV framework for the dog population to analyze rabies transmission patterns. The human population is categorized into four compartments: Susceptible, exposed, infected, and recovered. The dog population is classified into susceptible, exposed, infected, and vaccinated groups. Individuals classified as susceptible are not yet infected but are at risk of contracting rabies through interactions with rabid dogs. Exposed individuals have acquired the virus, typically through bites or scratches, but do not yet show clinical symptoms. Infected individuals exhibit symptoms of the disease, while the recovered category includes those who have undergone treatment and returned to a non-infectious state. Without proper intervention, exposed individuals may advance to the infectious phase and, ultimately, succumb to rabies.

The human population is modeled using four compartments: S_h (susceptible), E_h (exposed), I_h (infectious), and R_h (recovered). Individuals are initially recruited into the susceptible category. If a rabid dog bites a susceptible individual, they move to the exposed compartment. Without timely post-exposure prophylaxis, the individual progresses to the infectious stage and eventually succumbs to the disease, as recovery is not possible during the infectious phase.

Similarly, the dog population is structured into the compartments S_d (susceptible), E_d (exposed), I_d (infectious), and V_d (vaccinated). Dogs are added to the susceptible group at a recruitment rate φ_d. Treatment of susceptible dogs is implemented to prevent the disease from advancing. If no intervention is applied during the exposure phase, an exposed dog transitions directly to the infectious category.

The SEIR framework operates under the following assumptions:

- The recruitment rates of susceptible individuals for humans and dogs are represented by Λ_h and Λ_d, respectively.
- Transmission of rabies among humans is considered.
- Individuals who come into contact with a rabid dog through bites or scratches move into either the exposed or infected category.
- All compartments share a uniform natural death rate.

Based on the stated assumptions and the relationships among the variables and parameters, as illustrated in Figure 2, the dynamics of rabies transmission are formulated using ordinary differential equations. The SEIR framework offers a robust method for analyzing rabies transmission dynamics:

$$
\begin{aligned}
&{}^{\mathcal{ABC}}\mathbf{D}_t^{\xi} S_h(t) = \Lambda_h + \omega_h R_h(t) - (\beta_{h1} S_h(t) I_h(t) + \beta_{h2} S_h(t) I_d(t)) - \mu_h S_h(t),\\
&{}^{\mathcal{ABC}}\mathbf{D}_t^{\xi} E_h(t) = (\beta_{h1} S_h(t) I_h(t) + \beta_{h2} S_h(t) I_d(t)) - (\varphi_h + \rho_h + \mu_h) E_h(t),\\
&{}^{\mathcal{ABC}}\mathbf{D}_t^{\xi} I_h(t) = \rho_h E_h(t) - (\mu_h + \sigma_h) I_h(t),\\
&{}^{\mathcal{ABC}}\mathbf{D}_t^{\xi} R_h(t) = \varphi_h E_h(t) - (\omega_h + \mu_h) R_h(t),\\
&{}^{\mathcal{ABC}}\mathbf{D}_t^{\xi} S_d(t) = \Lambda_d - \beta_d S_d(t) I_d(t) + \omega_d V_d(t) - (\varphi_d + \mu_d) S_d(t),\\
&{}^{\mathcal{ABC}}\mathbf{D}_t^{\xi} E_d(t) = \beta_d S_d(t) I_d(t) - (\rho_d + \mu_d) E_d(t),\\
&{}^{\mathcal{ABC}}\mathbf{D}_t^{\xi} I_d(t) = \rho_d E_d(t) - (\mu_d + \sigma_d) I_d(t),\\
&{}^{\mathcal{ABC}}\mathbf{D}_t^{\xi} V_d(t) = \varphi_d S_d(t) - (\omega_d + \mu_d) V_d(t),\\
&S_h(0) = S_{h_0}, E_h(0) = E_{h_0}, I_h(0) = I_{h_0}, R_h(0) = R_{h_0}, S_d(0) = S_{d_0}, E_d(0) = E_{d_0}, I_d(0) = I_{d_0}, V_d(0) = V_{d_0}.
\end{aligned}
\tag{2.5}
$$

The analyzed system's positivity, feasibility, and stability can be evaluated by considering all compartments, as shown in [23].

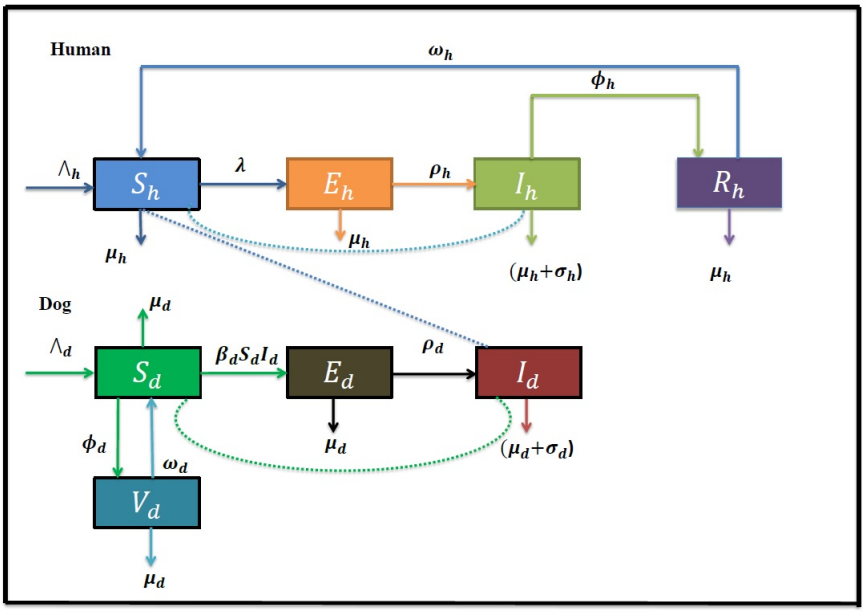

Figure 2. The flow diagram of model (2.5).

The parameters used in the proposed system are provided in Table 1.

Table 1. Parameters used in the numerical simulations of the model (2.5).

Parameter	Description
$S_h(t)$	Number of susceptible humans at time t
$E_h(t)$	Number of exposed humans at time t
$I_h(t)$	Number of infected humans at time t
$R_h(t)$	Number of recovered humans at time t
$S_d(t)$	Number of susceptible dogs at time t
$E_d(t)$	Number of exposed dogs at time t
$I_d(t)$	Number of infected dogs at time t
$V_d(t)$	Number of vaccinated dogs at time t
$N_h(t)$	Total human population size at time t
$N_d(t)$	Total dog population size at time t
Λ_h, Λ_d	Recruitment rates for human and dog populations, respectively
σ_h, σ_d	Rabies-induced death rates for humans and dogs, respectively
μ_h, μ_d	Natural death rates of human and dog populations, respectively
ρ_h, ρ_d	Incubation periods for humans and dogs, respectively
φ_h	Treatment rate for exposed humans
φ_d	Vaccination rate for susceptible dogs
ω_h, ω_d	Immunity loss rates for vaccinated humans and dogs, respectively

The study presents a fractional framework for analyzing rabies dynamics, utilizing a system of twelve compartments. The Atangana-Baleanu-Caputo operator is incorporated to enhance the modeling accuracy. The investigation ensures the existence and uniqueness of solutions for the initial value problem (IVP) within this structure. The robustness of the model is evaluated through the Ulam-Hyers stability concept. To approximate solutions, Newton's interpolation method is applied, allowing for the introduction of a fractional parameter to improve the numerical simulations across five compartments. This approach provides a comprehensive representation of the total density, spanning the range from 0 to 1.

3. Existence theory

This section discusses the significance of the proposed model in practical applications. Furthermore, an analysis of the stability and existence properties that are relevant to the underlying problem is provided. On the basis of these considerations, the problem is reformulated as follows:

$$\begin{cases} {}^{\mathcal{ABC}}\mathbf{D}_t^{\xi} S_h(t) &= \mathbf{G}_1(S_h, E_h, I_h, R_h, S_d, E_d, I_d, V_d), \\ {}^{\mathcal{ABC}}\mathbf{D}_t^{\xi} E_h(t) &= \mathbf{G}_3(S_h, E_h, I_h, R_h, S_d, E_d, I_d, V_d), \\ {}^{\mathcal{ABC}}\mathbf{D}_t^{\xi} I_h(t) &= \mathbf{G}_4(S_h, E_h, I_h, R_h, S_d, E_d, I_d, V_d), \\ {}^{\mathcal{ABC}}\mathbf{D}_t^{\xi} R_h(t) &= \mathbf{G}_5(S_h, E_h, I_h, R_h, S_d, E_d, I_d, V_d), \\ {}^{\mathcal{ABC}}\mathbf{D}_t^{\xi} S_d(t) &= \mathbf{G}_6(S_h, E_h, I_h, R_h, S_d, E_d, I_d, V_d), \\ {}^{\mathcal{ABC}}\mathbf{D}_t^{\xi} E_d(t) &= \mathbf{G}_7(S_h, E_h, I_h, R_h, S_d, E_d, I_d, V_d), \\ {}^{\mathcal{ABC}}\mathbf{D}_t^{\xi} I_d(t) &= \mathbf{G}_8(S_h, E_h, I_h, R_h, S_d, E_d, I_d, V_d). \end{cases} \tag{3.1}$$

We write Eq (2.5) in the form

$$\begin{aligned} {}^{\mathcal{ABC}}\mathbf{D}_t^{\xi} \mathbf{U}(t) &= \eta(t, \mathbf{U}(t)), \\ \mathbf{U}(0) &= \mathbf{U}_0(t), \end{aligned} \tag{3.2}$$

where

$$\begin{cases} \mathbf{U}(t) := (S_h, E_h, I_h, R_h, S_d, E_d, I_d, V_d)^T, \\ \mathbf{U}_0 := (S_{h_0}, E_{h_0}, I_{h_0}, R_{h_0}, S_{d_0}, E_{d_0}, I_{d_0}, V_{d_0})^T, \\ \eta(t, \mathbf{U}(t)) := \mathbf{G}_i(t, S_h, E_h, I_h, R_h, S_d, E_d, I_d, V_d)^T, \quad i = 1, 2, 3, 4, 5, 6, 7, 8. \end{cases} \tag{3.3}$$

Here, $(.)^T$ represents the transpose of a vector. The integral formulation of the equation in system (3.2) can be written as:

$$\mathbf{U}(t) = \mathbf{U}_0 + \frac{1-\xi}{M(\xi)} Z(t, \mathbf{U}(t)) + \frac{\xi}{M(\xi)\Gamma(\xi)} \int_0^t (t-\varphi)^{\xi-1} Z(\varphi, \mathbf{U}(\varphi))\, d\varphi. \tag{3.4}$$

Let $\Upsilon = C([0, T], \mathbf{R}^k)_{1\le k\le n}$ be a Banach space equipped with the norm $\|\mathbf{U}\| = \sup_{t\in[0,T]} |\mathbf{U}(t)|$. Moreover, define $\Phi = (\Upsilon^8, \|\mathbf{U}\|)$ as another Banach space, where the norm $\|\mathbf{U}\|$ is specified as:

$$\|\mathbf{U}\| = \sup_{t\in[0,T]} (|S_h| + |E_h| + |I_h| + |R_h| + |S_d| + |E_d| + |I_d| + |V_d|). \tag{3.5}$$

The existence results are established in the following theorem using Schauder's fixed-point theorem.

Theorem 3.1. *Let $Z \in \Phi$ be a continuously defined function, and suppose that a positive constant $V > 0$ exists that the inequality,*

$$|Z(t, \mathbf{U}(t))| \le V(1 + |\mathbf{U}|)$$

holds for all $t \in [0, T]$ and $\mathbf{U} \in \Phi$. Under this condition, the following inequality is satisfied:

$$\nabla_1 = \left(\frac{(1-\xi)\Gamma(\xi)V + VT^{\xi}}{M(\xi)\Gamma(\xi)} \right) < 1. \tag{3.6}$$

Consequently, the solution of Eq (3.4) *is well-defined, unique, and continuous for every $t \in [0, T]$.*

Proof. The solution of the stated problem adheres to the equivalent integral form given in Eq (3.4). Define the operator $\mho : \Phi \to \Phi$ as follows:

$$(\mho \mathbf{U})(t) = \mathbf{U}_0 + \frac{1-\xi}{M(\xi)} Z(t, \mathbf{U}(t)) + \frac{\xi}{M(\xi)\Gamma(\xi)} \int_0^t (t-\varphi)^{\xi-1} Z(\lambda, \mathbf{U}(\lambda)) d\lambda. \tag{3.7}$$

Consider a closed, bounded, and convex ball $\mathbb{B}_\varrho$ defined as $\{\mathbf{U} \in \lambda : \|\mathbf{U}\| \leq \varrho, \varrho > 0\}$, where

$$\varrho \geq \frac{\nabla_2}{1-\nabla_1}, \quad \text{and} \quad \nabla_2 = |\mathbf{U}_0| + \frac{1-\xi}{M(\xi)}V + \frac{T^\xi}{M(\xi)\Gamma(\xi)}V. \tag{3.8}$$

To verify the required condition, it suffices to show that $(\mho)(\mathbb{B}_\varrho) \subset \mathbb{B}_\varrho$ for every $t \in [0,T]$. Consequently, we obtain

$$\begin{aligned} |(\mho\mathbf{U})(t)| &\leq |\mathbf{U}_0| + \frac{1-\xi}{M(\xi)}|Z(t,\mathbf{U}(t))| + \frac{\xi}{M(\xi)\Gamma(\xi)}\int_0^t (t-\lambda)^{\xi-1}|Z(\lambda,\mathbf{U}(\lambda))|d\lambda \\ &\leq |\mathbf{U}_0| + \frac{1-\xi}{M(\xi)}V(1+|\mathbf{U}(t)|) + \frac{\xi}{M(\xi)\Gamma(\xi)}\int_0^t (t-\lambda)^{\xi-1}V(1+|\mathbf{U}(t)|)d\lambda, \end{aligned} \tag{3.9}$$

and $\mathbf{U} \in \mathbb{B}_\varrho$. We also obtain

$$\begin{aligned} \|(\mho\mathbf{U})\| &\leq |\mathbf{U}_0| + \frac{1-\xi}{M(\xi)}V(1+\|\mathbf{U}(t)\|) + \frac{T^\xi}{M(\xi)\Gamma(\xi)}V(1+\|\mathbf{U}(t)\|) \\ &\leq |\mathbf{U}_0| + \frac{1-\xi}{M(\xi)}V + \frac{T^\xi}{M(\xi)\Gamma(\xi)}V + \left[\frac{1-\xi}{M(\xi)}V + \frac{T^\xi}{M(\xi)\Gamma(\xi)}V\right]\varrho \\ &\leq \nabla_2 + \nabla_1\varrho \leq \varrho. \end{aligned}$$

We have established that $(\mho\mathbb{B}_\varrho) \subset \mathbb{B}_\varrho$.

To establish the continuity of the operator $\mho$, consider a sequence $\{\mathbf{U}_n\}$ such that $\mathbf{U}_n$ converges to $\mathbf{U}$ in $\mathbb{B}_\varrho$ as $n \to \infty$. Consequently, for any $t \in [0,T]$, the following condition is satisfied:

$$\begin{aligned} \left|(\mho\mathbf{U}_n)(t) - (\mho\mathbf{U})(t)\right| &\leq \frac{1-\xi}{M(\xi)}\left|Z(t,\mathbf{U}_n(t)) - Z(t,\mathbf{U}(t))\right| + \\ &\quad \frac{\xi}{M(\xi)\Gamma(\xi)}\int_0^t (t-\lambda)^{\xi-1}\left|Z(\lambda,\mathbf{U}_n(\lambda)) - Z(\lambda,\mathbf{U}(\lambda))\right|d\lambda \\ &\leq \frac{1-\xi}{M(\xi)}\|Z(t,\mathbf{U}_n(t)) - Z(t,\mathbf{U}(t))\| \\ &+ \frac{T^\xi}{M(\xi)\Gamma(\xi)}\|Z(\lambda,\mathbf{U}_n(\lambda)) - Z(y,\mathbf{U}(\lambda))\|. \end{aligned}$$

Due to the continuity of the function Z, the following holds:

$$\|(\mho\mathbf{U}_n)(t) - (\mho\mathbf{U})(t)\| \to 0 \quad \text{as} \quad n \to \infty. \tag{3.10}$$

The operator $\mho$ is proven to be continuous over $\mathbb{B}_\varrho$. Furthermore, it can be established that $(\mho\mathbb{B}_\varrho)$ possesses relative compactness. Since $(\mho\mathbb{B}_\varrho) \subset \mathbb{B}_\varrho$, the set $(\mho\mathbb{B}_\varrho)$ remains uniformly bounded. In addition, we demonstrate that $\mho$ satisfies the criterion of "equi-continuity" within $\mathbb{B}_\varrho$. Given $\mathbf{U} \in \mathbb{B}_\varrho$ and two points $t_1, t_2 \in [0,T]$ where $t_1 < t_2$, the subsequent result follows:

$$\begin{aligned} \|\mho\mathbf{U}(t_2) - \mho\mathbf{U}(t_1)\| &\leq \frac{1-\xi}{M(\xi)}\left|Z(t_2,\mathbf{U}(t_2)) - Z(t_1,\mathbf{U}(t_1))\right| \\ &+ \frac{\xi}{M(\xi)\Gamma(\xi)}\left|\left[\int_0^{t_2}(t_2-\lambda)^{\xi-1} - \int_0^{t_1}(t_1-\lambda)^{\xi-1}\right]Z(\lambda,\mathbf{U}(\lambda))d\lambda\right| \end{aligned}$$

$$\leq \frac{1-\xi}{M(\xi)}\big|Z(t_2,\mathbf{U}(t_2))-Z(t_1,\mathbf{U}(t_1))\big|+\frac{\xi}{M(\xi)}\frac{L(1+\|\mathbf{U}\|)}{\Gamma(\xi+1)}(t_2^{\xi}-t_1^{\xi}).$$

It is evident that the norm $\|\mho\mathbf{U}(t_2)-\mho\mathbf{U}(t_1)\|$ approaches zero as t_2 tends to t_1. Using the Arzelà-Ascoli theorem, it follows that $(\mho\mathbb{B}_{\varrho})$ is relatively compact, which implies that the operator is completely continuous. As a result, the formulation in (2.5) guarantees the existence of at least one solution.

Next, we investigate the conditions ensuring the uniqueness of the solution corresponding to the proposed model (2.5), subject to the following assumption:

$$0\leq\Big[1-\frac{1-\xi}{M(\xi)}\varrho-\frac{\xi T^{\xi}}{M(\xi)\Gamma(\xi)}\varrho\Big]. \tag{3.11}$$

Assume there are additional solutions, denoted by $S_h(t), E_h(t), I_h(t), R_h(t), S_d(t), E_d(t), I_d(t), and V_d(t)$; it then follows that

$$S_h(t)-S_{h_1}(t)=\frac{1-\xi}{M(\xi)}(\mathbf{F}_1(t,S_h(t))-\mathbf{F}_1(t,S_h(t)))+\frac{\xi}{M(\xi)\Gamma(\xi)}\int_0^t(\mathbf{F}_1(\lambda,S_h)-\mathbf{F}_1(\lambda,S_{h_1}(t)))d\lambda. \tag{3.12}$$

Using the norm to Eq (3.12), we have

$$\begin{aligned}\big\|S_h(t)-S_{h_1}(t)\big\| &= \Big\|\frac{1-\xi}{M(\xi)}(\mathbf{F}_1(t,S_h(t))-\mathbf{F}_1(t,S_{h_1}(t)))+\frac{\xi}{M(\xi)\Gamma(\xi)}\int_0^t(\mathbf{F}_1(\lambda,S_h(t))-\mathbf{F}_1(\lambda,S_{h_1}(t)))d\lambda\Big\|\\ &\leq \frac{1-\xi}{M(\xi)}\varrho\big\|S_h(t)-S_{h_1}(t)\big\|+\frac{\xi}{M(\xi)\Gamma(\xi)}\varrho\big\|S_h(t)-S_{h_1}(t)\big\|. \end{aligned}\tag{3.13}$$

Therefore,

$$\big\|S_h(t)-S_{h_1}(t)\big\|\Big[1-\frac{1-\xi}{M(\xi)}\varrho-\frac{\xi T^{\xi}}{M(\xi)\Gamma(\xi)}\varrho\Big]\leq 0. \tag{3.14}$$

This implies that $S_h(t) = S_{h_1}(t)$ if the inequality (3.11) is satisfied. Similarly, for the other compartments, we have $E_h(t) = E_{h_1}(t)$, $I_h(t) = I_{h_1}(t)$, $R_h(t) = R_{h_1}(t)$, $S_d(t) = S_{d_1}(t)$, $E_d(t) = E_{d_1}(t)$, $I_d(t) = I_{d_1}(t)$, and $V_d(t) = V_{d_1}(t)$. Therefore, the solution is unique. □

Proceeding further, we analyze the Ulam–Hyers stability characteristics associated with the system described in (2.5).

Theorem 3.2. *Let $Z \in \lambda$ be continuously defined function, and let $\mathcal{K} > 0$ be a given constant such that the inequality*

$$\big|Z(t,\mathbf{Q})-Z(t,\widetilde{\mathbf{Q}})\big|\leq\mathcal{K}\big|\mathbf{Q}-\widetilde{\mathbf{Q}}\big|$$

holds for all $t \in [0, T]$ and $\mathbf{Q} \in \lambda$. Additionally, assume that the condition

$$1>\frac{(1-\xi)\Gamma(\xi)\mathcal{K}+\mathcal{K}T^{\xi}}{M(\xi)\Gamma(\xi)}$$

is satisfied. Let $\mathbf{Q}$ and $\widetilde{\mathbf{Q}}$ be the solutions of Eq (3.2),

$${}^{\mathcal{ABC}}\mathbf{D}_t^{\xi}\tilde{\mathbf{Q}}(t)=Z(t,\tilde{\mathbf{Q}}(t)),\quad \tilde{\mathbf{Q}}(0)=\mathbf{Q}_0+\varepsilon\geq 0, \tag{3.15}$$

where

$$\begin{cases} \tilde{\mathbf{Q}} = (\tilde{S}_h, \tilde{E}_h, \tilde{I}_h, \tilde{R}_h, \tilde{S}_d, \tilde{E}_d, \tilde{I}_d, \tilde{V}_d)^T, \\ \mathbf{Q}_0 + \varepsilon = (S_{h_0} + \varepsilon, E_{h_0} + \varepsilon, I_{h_0} + \varepsilon, R_{h_0} + \varepsilon, S_{d_0} + \varepsilon + E_{d_0} + \varepsilon, I_{d_0} + \varepsilon, V_{d_0} + \varepsilon)^T, \\ Z(t, \tilde{\mathbf{Q}}(t)) = \mathbf{F}_i(\tilde{S}_h, \tilde{E}_h, \tilde{I}_h, \tilde{R}_h, \tilde{S}_d, \tilde{E}_d, \tilde{I}_d, \tilde{V}_d)^T, \quad i = 1, 2, 3, 4, 5, 6, 7, 8. \end{cases} \tag{3.16}$$

Then,

$$\|\mathbf{Q} - \tilde{\mathbf{Q}}\| \leq \left[1 - \frac{(1-\xi)\Gamma(\xi)\mathcal{K} + \mathcal{K}T^{\xi}}{M(\xi)\Gamma(\xi)}\right]^{-1} |\varepsilon|. \tag{3.17}$$

Proof. The formulation of the given problem (3.2), along with Eq (3.15), leads to an equivalent integral representation given by Eq (3.4), which can be expressed as follows:

$$\tilde{\mathbf{Q}}(t) = \mathbf{Q}_0 + \varepsilon + \frac{1-\xi}{M(\xi)} Z(t, \tilde{\mathbf{Q}}(t)) + \frac{\xi}{M(\xi)\Gamma(\xi)} \int_0^t (t-\lambda)^{\xi-1} Z(\lambda, \tilde{\mathbf{Q}}(\lambda)) d\lambda. \tag{3.18}$$

For any $t \in [0, T]$, the following inequality holds:

$$\begin{aligned} |\mathbf{Q}(t) - \tilde{\mathbf{Q}}(t)| &\leq |\varepsilon| + \frac{1-\xi}{M(\xi)} \left| Z(t, \mathbf{Q}(t)) - Z(t, \tilde{\mathbf{Q}}(t)) \right| \\ &+ \frac{\xi}{M(\xi)\Gamma(\xi)} \int_0^t (t-\lambda)^{\xi-1} \left| Z(\lambda, \mathbf{Q}(\lambda)) - Z(\lambda, \tilde{\mathbf{Q}}(\lambda)) \right| d\lambda \\ &\leq |\varepsilon| + \frac{1-\xi}{M(\xi)} \mathcal{K} \left| \mathbf{Q}(t) - \tilde{\mathbf{Q}}(t) \right| + \frac{\xi}{M(\xi)\Gamma(\xi)} \int_0^t (t-\lambda)^{\xi-1} \mathcal{K} \left| \mathbf{Q}(\lambda) - \tilde{\mathbf{Q}}(\lambda) \right| d\lambda \\ &\leq |\varepsilon| + \left[\frac{1-\xi}{M(\xi)} + \frac{T^{\xi}}{M(\xi)\Gamma(\xi)} \right] \mathcal{K} \|\mathbf{Q} - \tilde{\mathbf{Q}}\|. \end{aligned}$$

Thus, we arrive at the following:

$$\|\mathbf{Q} - \tilde{\mathbf{Q}}\| \leq |\varepsilon| + \left[\frac{(1-\xi)\Gamma(\xi) + T^{\xi}}{M(\xi)\Gamma(\xi)} \right] \mathcal{K} \|\mathbf{Q} - \tilde{\mathbf{Q}}\|.$$

Therefore,

$$\|\mathbf{Q} - \tilde{\mathbf{Q}}\| \leq \left[1 - \frac{(1-\xi)\Gamma(\xi)\mathcal{K} + \mathcal{K}T^{\xi}}{M(\xi)\Gamma(\xi)}\right]^{-1} |\varepsilon|.$$

This completes the proof of the theorem. □

4. Numerical approach

In this section, we present a computational approach to address the problem at hand. The temporal derivative is expressed in terms of a fractional derivative incorporating the Mittag-Leffler (ML) kernel. The adopted strategy includes executing a numerical simulation facilitated by an interpolation polynomial. Furthermore, the Adams-Bashforth (AB) scheme is employed to estimate the fractional-order integral, as it is a widely recognized numerical technique [13].

By incorporating the initial conditions and utilizing the operator ${}^{\mathcal{ABC}}\mathbf{I}_0^{\xi}$, we apply the outlined scheme to the problem under consideration. The formulation is as follows:

$$\begin{cases} S_h(t) - S_{h_0} &= {}^{\mathcal{ABC}}\mathbf{I}_0^{\xi}\mathbf{G}_1(S_h, t), \\ E_h(t) - E_{h_0} &= {}^{\mathcal{ABC}}\mathbf{I}_0^{\xi}\mathbf{G}_2(E_h, t), \\ I_h(t) - I_{h_0} &= {}^{\mathcal{ABC}}\mathbf{E}_0^{\xi}\mathbf{G}_3(I_h, t), \\ R_h(t) - R_{h_0} &= {}^{\mathcal{ABC}}\mathbf{I}_0^{\xi}\mathbf{G}_4(R_h, t), \\ S_d(t) - S_{d_0} &= {}^{\mathcal{ABC}}\mathbf{I}_0^{\xi}\mathbf{G}_5(S_d, t), \\ E_d(t) - E_{d_0} &= {}^{\mathcal{ABC}}\mathbf{I}_0^{\xi}\mathbf{G}_6(E_d, t), \\ I_d(t) - I_{d_0} &= {}^{\mathcal{ABC}}\mathbf{I}_0^{\xi}\mathbf{G}_7(I_d, t), \\ V_d(t) - V_{d_0} &= {}^{\mathcal{ABC}}\mathbf{I}_0^{\xi}\mathbf{G}_8(V_d, t), \end{cases} \tag{4.1}$$

which gives

$$\begin{aligned} S_h(t) - S_{h_0} &= \frac{1-\xi}{M(\xi)}\mathbf{G}_1(S_h(t), t) + \frac{\xi}{M(\xi)\Gamma(\xi)}\int_0^t (t-\lambda)^{\xi-1}\mathbf{G}_1(S_h(\lambda), \lambda)d\lambda, \\ E_h(t) - E_{h_0} &= \frac{1-\xi}{M(\xi)}\mathbf{G}_2(E_h(t), t) + \frac{\xi}{M(\xi)\Gamma(\xi)}\int_0^t (t-\lambda)^{\xi-1}\mathbf{G}_2(E_h(\lambda), \lambda)d\lambda, \\ I_h(t) - I_{h_0} &= \frac{1-\xi}{M(\xi)}\mathbf{G}_3(I_h(t), t) + \frac{\xi}{M(\xi)\Gamma(\xi)}\int_0^t (t-\lambda)^{\xi-1}\mathbf{G}_3(I_h(\lambda), \lambda)d\lambda, \\ R_h(t) - R_{h_0} &= \frac{1-\xi}{M(\xi)}\mathbf{G}_4(R_h(t), t) + \frac{\xi}{M(\xi)\Gamma(\xi)}\int_0^t (t-\lambda)^{\xi-1}\mathbf{G}_4(R_h(\lambda), \lambda)d\lambda, \\ S_d(t) - S_{d_0} &= \frac{1-\xi}{M(\xi)}\mathbf{G}_5(S_d(t), t) + \frac{\xi}{M(\xi)\Gamma(\xi)}\int_0^t (t-\lambda)^{\xi-1}\mathbf{G}_5(S_d(\lambda), \lambda)d\lambda, \\ E_d(t) - E_{d_0} &= \frac{1-\xi}{M(\xi)}\mathbf{G}_6(E_d(t), t) + \frac{\xi}{M(\xi)\Gamma(\xi)}\int_0^t (t-\lambda)^{\xi-1}\mathbf{G}_6(E_d(\lambda), \lambda)d\lambda, \\ I_d(t) - I_{d_0} &= \frac{1-\xi}{M(\xi)}\mathbf{G}_7(I_d(t), t) + \frac{\xi}{M(\xi)\Gamma(\xi)}\int_0^t (t-\lambda)^{\xi-1}\mathbf{G}_7(I_d(\lambda), \lambda)d\lambda, \\ V_d(t) - V_{d_0} &= \frac{1-\xi}{M(\xi)}\mathbf{G}_8(V_d(t), t) + \frac{\xi}{M(\xi)\Gamma(\xi)}\int_0^t (t-\lambda)^{\xi-1}\mathbf{G}_8(V_d(\lambda), \lambda)d\lambda. \end{aligned}$$

To develop an iterative process, we substitute t with $t_{\xi+1}$ for $\xi = 0, 1, 2, \ldots$ in the proposed system:

$$
\begin{cases}
S_h(t_{\xi+1}) - S_h(0) &= \frac{1-\xi}{M(\xi)}\mathbf{G}_1(S_h(t_\xi), t_\xi) + \frac{\xi}{M(\xi)\Gamma(\xi)}\sum_{i=0}^{\xi}\int_{t_i}^{t_{i+1}}(t_{\xi+1}-\lambda)^{\xi-1}\mathbf{G}_1(S_h(\lambda),\lambda)d\lambda,\\
E_h(t_{\xi+1}) - E_h(0) &= \frac{1-\xi}{M(\xi)}\mathbf{G}_2(E_h(t_\xi), t_\xi) + \frac{\xi}{M(\xi)\Gamma(\xi)}\sum_{i=0}^{\xi}\int_{t_i}^{t_{i+1}}(t_{\xi+1}-\lambda)^{\xi-1}\mathbf{G}_2(E_h(\lambda),\lambda)d\lambda,\\
I_h(t_{\xi+1}) - I_h(0) &= \frac{1-\xi}{M(\xi)}\mathbf{G}_3(I_h(t_\xi), t_\xi) + \frac{\xi}{M(\xi)\Gamma(\xi)}\sum_{i=0}^{\xi}\int_{t_i}^{t_{i+1}}(t_{\xi+1}-\lambda)^{\xi-1}\mathbf{G}_3(I_h(\lambda),\lambda)d\lambda,\\
R_h(t_{\xi+1}) - R_h(0) &= \frac{1-\xi}{M(\xi)}\mathbf{G}_4(R_h(t_\xi), t_\xi) + \frac{\xi}{M(\xi)\Gamma(\xi)}\sum_{i=0}^{\xi}\int_{t_i}^{t_{i+1}}(t_{\xi+1}-\lambda)^{\xi-1}\mathbf{G}_4(R_h(\lambda),\lambda)d\lambda,\\
S_d(t_{\xi+1}) - S_d(0) &= \frac{1-\xi}{M(\xi)}\mathbf{G}_5(S_d(t_\xi), t_\xi) + \frac{\xi}{M(\xi)\Gamma(\xi)}\sum_{i=0}^{\xi}\int_{t_i}^{t_{i+1}}(t_{\xi+1}-\lambda)^{\xi-1}\mathbf{G}_5(S_d(\lambda),\lambda)d\lambda,\\
E_d(t_{\xi+1}) - E_d(0) &= \frac{1-\xi}{M(\xi)}\mathbf{G}_6(E_d(t_\xi), t_\xi) + \frac{\xi}{M(\xi)\Gamma(\xi)}\sum_{i=0}^{\xi}\int_{t_i}^{t_{i+1}}(t_{\xi+1}-\lambda)^{\xi-1}\mathbf{G}_6(E_d(\lambda),\lambda)d\lambda,\\
I_d(t_{\xi+1}) - I_d(0) &= \frac{1-\xi}{M(\xi)}\mathbf{G}_7(I_d(t_\xi), t_\xi) + \frac{\xi}{M(\xi)\Gamma(\xi)}\sum_{i=0}^{\xi}\int_{t_i}^{t_{i+1}}(t_{\xi+1}-\lambda)^{\xi-1}\mathbf{G}_7(I_d(\lambda),\lambda)d\lambda,\\
V_d(t_{\xi+1}) - V_d(0) &= \frac{1-\xi}{M(\xi)}\mathbf{G}_8(V_d(t_\xi), t_\xi) + \frac{\xi}{M(\xi)\Gamma(\xi)}\sum_{i=0}^{\xi}\int_{t_i}^{t_{i+1}}(t_{\xi+1}-\lambda)^{\xi-1}\mathbf{G}_8(V_d(\lambda),\lambda)d\lambda.
\end{cases}
$$

To approximate the functions $\mathbf{G}_1(S_h(\lambda),\lambda)$, $\mathbf{G}_2(E_h(\lambda),\lambda)$, $\mathbf{G}_3(I_h(\lambda),\lambda)$, $\mathbf{G}_4(R_h(\lambda),\lambda)$, $\mathbf{G}_5(S_d(\lambda),\lambda)$, $\mathbf{G}_6(E_d(\lambda),\lambda)$, $\mathbf{G}_7(I_d(\lambda),\lambda)$, and $\mathbf{G}_8(V_d(\lambda),\lambda)$, a two-step interpolation polynomial is applied. This is performed within the integral on the interval $[t_i, t_{i+1}]$, leading to the following expression:

$$
\begin{cases}
\mathbf{G}_1(S_h(\lambda),\lambda) &\cong \frac{\mathbf{G}_1(S_h(t_i),t_i)}{\Delta}(t-t_{i-1}) + \frac{\mathbf{G}_1(S_h(t_{i-1}),t_{i-1})}{\Delta}(t-t_i),\\
\mathbf{G}_2(E_h(\lambda),\lambda) &\cong \frac{\mathbf{G}_2(E_h(t_i),t_i)}{\Delta}(t-t_{i-1}) + \frac{\mathbf{G}_2(E_h(t_{i-1}),t_{i-1})}{\Delta}(t-t_i),\\
\mathbf{G}_3(I_h(\lambda),\lambda) &\cong \frac{\mathbf{G}_3(I_h(t_i),t_i)}{\Delta}(t-t_{i-1}) + \frac{\mathbf{G}_3(I_h(t_{i-1}),t_{i-1})}{\Delta}(t-t_i),\\
\mathbf{G}_4(R_h(\lambda),\lambda) &\cong \frac{\mathbf{G}_4(R_h(t_i),t_i)}{\Delta}(t-t_{i-1}) + \frac{\mathbf{G}_4(R_h(t_{i-1}),t_{i-1})}{\Delta}(t-t_i),\\
\mathbf{G}_5(S_d(\lambda),\lambda) &\cong \frac{\mathbf{G}_5(S_d(t_i),t_i)}{\Delta}(t-t_{i-1}) + \frac{\mathbf{G}_5(S_d(t_{i-1}),t_{i-1})}{\Delta}(t-t_i),\\
\mathbf{G}_6(E_dS(\lambda),\lambda) &\cong \frac{\mathbf{G}_6(E_d(t_i),t_i)}{\Delta}(t-t_{i-1}) + \frac{\mathbf{G}_6(I_d(t_{i-1}),t_{i-1})}{\Delta}(t-t_i),\\
\mathbf{G}_7(I_d(\lambda),\lambda) &\cong \frac{\mathbf{G}_7(I_d(t_i),t_i)}{\Delta}(t-t_{i-1}) + \frac{\mathbf{G}_7(E_d(t_{i-1}),t_{i-1})}{\Delta}(t-t_i),\\
\mathbf{G}_8(V_d(\lambda),\lambda) &\cong \frac{\mathbf{G}_8(V_d(t_i),t_i)}{\Delta}(t-t_{i-1}) + \frac{\mathbf{G}_8(V_d(t_{i-1}),t_{i-1})}{\Delta}(t-t_i),
\end{cases}
\tag{4.2}
$$

which gives

$$
\begin{aligned}
S_h(t_{j+1}) &= S_h(0) + \frac{1-\xi}{M(\xi)}\mathbf{G}_1(S_h(t_j), t_j) + \frac{\xi}{M(\xi)\Gamma(\xi)}\sum_{i=0}^{\nu}\left(\frac{\mathbf{G}_1(S_h(t_i), t_i)}{\Delta}\mathcal{I}_{i-1,\xi} + \frac{\mathbf{G}_1(S_h(t_{i-1}), t_{i-1})}{\Delta}\mathcal{I}_{i,\xi}\right),\\
E_h(t_{j+1}) &= E_h(0) + \frac{1-\xi}{M(\xi)}\mathbf{G}_2(E_h(t_j), t_j) + \frac{\xi}{M(\xi)\Gamma(\xi)}\sum_{i=0}^{\nu}\left(\frac{\mathbf{G}_2(E_h(t_i), t_i)}{\Delta}\mathcal{I}_{i-1,\xi} + \frac{\mathbf{G}_2(E_h(t_{i-1}), t_{i-1})}{\Delta}\mathcal{I}_{i,\xi}\right),\\
I_h(t_{j+1}) &= I_h(0) + \frac{1-\xi}{M(\xi)}\mathbf{G}_3(I_h(t_j), t_j) + \frac{\xi}{M(\xi)\Gamma(\xi)}\sum_{i=0}^{\nu}\left(\frac{\mathbf{G}_3(I_h(t_i), t_i)}{\Delta}\mathcal{I}_{i-1,\xi} + \frac{\mathbf{G}_3(I_h(t_{i-1}), t_{i-1})}{\Delta}\mathcal{I}_{i,\xi}\right),\\
R_h(t_{j+1}) &= R_h(0) + \frac{1-\xi}{M(\xi)}\mathbf{G}_4(R_h(t_j), t_j) + \frac{\xi}{M(\xi)\Gamma(\xi)}\sum_{i=0}^{\nu}\left(\frac{\mathbf{G}_4(R_h(t_i), t_i)}{\Delta}\mathcal{I}_{i-1,\xi} + \frac{\mathbf{G}_4(R_h(t_{i-1}), t_{i-1})}{\Delta}\mathcal{I}_{i,\xi}\right),\\
S_d(t_{j+1}) &= S_d(0) + \frac{1-\xi}{M(\xi)}\mathbf{G}_5(S_d(t_j), t_j) + \frac{\xi}{M(\xi)\Gamma(\xi)}\sum_{i=0}^{\nu}\left(\frac{\mathbf{G}_5(S_d(t_i), t_i)}{\Delta}\mathcal{I}_{i-1,\xi} + \frac{\mathbf{G}_5(S_d(t_{i-1}), t_{i-1})}{\Delta}\mathcal{I}_{i,\xi}\right),\\
E_d(t_{j+1}) &= E_d(0) + \frac{1-\xi}{M(\xi)}\mathbf{G}_6(E_d(t_j), t_j) + \frac{\xi}{M(\xi)\Gamma(\xi)}\sum_{i=0}^{\nu}\left(\frac{\mathbf{G}_6(E_d(t_i), t_i)}{\Delta}\mathcal{I}_{i-1,\xi} + \frac{\mathbf{G}_6(E_d(t_{i-1}), t_{i-1})}{\Delta}\mathcal{I}_{i,\xi}\right),\\
I_d(t_{j+1}) &= I_d(0) + \frac{1-\xi}{M(\xi)}\mathbf{G}_7(I_d(t_j), t_j) + \frac{\xi}{M(\xi)\Gamma(\xi)}\sum_{i=0}^{\nu}\left(\frac{\mathbf{G}_7(I_d(t_i), t_i)}{\Delta}\mathcal{I}_{i-1,\xi} + \frac{\mathbf{G}_7(I_d(t_{i-1}), t_{i-1})}{\Delta}\mathcal{I}_{i,\xi}\right),\\
V_d(t_{j+1}) &= V_d(0) + \frac{1-\xi}{M(\xi)}\mathbf{G}_8(V_d(t_j), t_j) + \frac{\xi}{M(\xi)\Gamma(\xi)}\sum_{i=0}^{\nu}\left(\frac{\mathbf{G}_8(V_d(t_i), t_i)}{\Delta}\mathcal{I}_{i-1,\xi} + \frac{\mathbf{G}_8(V_d(t_{i-1}), t_{i-1})}{\Delta}\mathcal{I}_{i,\xi}\right),
\end{aligned}
\tag{4.3}
$$

where

$$
\mathcal{I}_{i-1,\xi} = \int_{t_i}^{t_{i+1}}(t-t_{i-1})(t_{j+1}-t)^{\xi-1}dt, \quad \mathcal{I}_{i,\xi} = \int_{t_i}^{t_{i+1}}(t-t_i)(t_{j+1}-t)^{\xi-1}dt.
$$

In this section, we evaluate the integrals $\mathcal{I}_{i-1,\xi}$ and $\mathcal{I}_{i,\xi}$ using the following approach:

$$
\begin{aligned}
\mathcal{I}_{i-1,\xi} &= -\frac{1}{\xi}\Big[(t_{i+1}-t_{i-1})(t_{j+1}-t_{i+1})^{\xi} - (t_i-t_{i-1})(t_{j+1}-t_i)^{\xi}\Big]\\
&\quad -\frac{1}{\xi(\xi-1)}\Big[(t_{j+1}-t_{i+1})^{\xi+1} - (t_{j+1}-t_i)^{\xi+1}\Big],
\end{aligned}
$$

and

$$
\mathcal{I}_{i,\xi} = -\frac{1}{\xi}\Big[(t_{i+1}-t_i)(t_{j+1}-t_{i+1})^{\xi}\Big] - \frac{1}{\xi(\xi-1)}\Big[(t_{\xi+1}-t_{j+1})^{\xi+1} - (t_{j+1}-t_i)^{\xi+1}\Big].
$$

Assuming $t_i = i\Delta$, it follows that:

$$
\mathcal{I}_{i-1,\xi} = -\frac{\Delta^{\xi+1}}{\xi(\xi+1)}\Big[(j+1-i)^{\xi}(-i+j+2+\xi) - (-i+j)^{\xi}(-i+2\xi+j+2)\Big], \tag{4.4}
$$

$$
\mathcal{I}_{i,\xi} = \frac{\Delta^{\xi+1}}{\xi(\xi+1)}\Big[(j+1-i)^{\xi+1} - (j-i)^{\xi}(j-i+1+\xi)\Big]. \tag{4.5}
$$

By inserting the results from Eqs (4.4) and (4.5) into Eq (4.3), the following is derived:

$$\begin{aligned}
S_h(t_{j+1}) &= S_h(t_0) + \frac{(1-\xi)}{M(\xi)}\Big[\mathbf{G}_1(S_h(t_j), t_J)\Big] + \frac{\xi}{M(\xi)}\sum_{i=0}^{j}\Big(\frac{\mathbf{G}_1(S_h(t_j), t_j)}{\Gamma(\xi+2)} \\
&\times\Delta^{\xi}\Big[(j+1-i)^{\xi}(j-i+2+\xi) - (j-i)^{\xi}(j-i+2+2\xi)\Big] \\
&-\frac{\mathbf{G}_1(S_h(t_{j-1}), t_{j-1})}{\xi(\xi+2)}\Delta^{\xi}[(j+1-i)^{\xi+1} - (j-i)^{\xi}(j-i+1+\xi)]\Big), \qquad (4.6)\\
E_h(t_{j+1}) &= E_h(t_0) + \frac{(1-\xi)}{M(\xi)}\Big[\mathbf{G}_2(E_h(t_j), t_j)\Big] + \frac{\xi}{M(\xi)}\sum_{i=0}^{j}\Big(\frac{\mathbf{G}_2(E_h(t_j), t_j)}{\Gamma(\xi+2)} \\
&\times\Delta^{\xi}\Big[(j+1-i)^{\xi}(j-i+2+\xi) - (j-i)^{\xi}(j-i+2+2\xi)\Big] \\
&-\frac{\mathbf{G}_2(E_h(t_{j-1}), t_{j-1})}{\xi(\xi+2)}\Delta^{\xi}[(\iota+1-i)^{\xi+1} - (j-i)^{\xi}(j-i+1+\xi)]\Big), \qquad (4.7)\\
I_h(t_{j+1}) &= I_h(t_0) + \frac{(1-\xi)}{M(\xi)}\Big[\mathbf{G}_3(I_h(t_j), t_j)\Big] + \frac{\xi}{M(\xi)}\sum_{i=0}^{j}\Big(\frac{\mathbf{G}_3(I_h(t_j), t_j)}{\Gamma(\xi+2)} \\
&\times\Delta^{\xi}\Big[(j+1-i)^{\xi}(j-i+2+\xi) - (j-i)^{\xi}(j-i+2+2\xi)\Big] \\
&-\frac{\mathbf{G}_3(I_h(t_{j-1}), t_{j-1})}{\xi(\xi+2)}\Delta^{\xi}[(j+1-i)^{\xi+1} - (j-i)^{\xi}(j-i+1+\xi)]\Big), \qquad (4.8)\\
R_h(t_{j+1}) &= R_h(t_0) + \frac{(1-\xi)}{M(\xi)}\Big[\mathbf{G}_4(R_h(t_j), t_j)\Big] + \frac{\xi}{M(\xi)}\sum_{i=0}^{j}\Big(\frac{\mathbf{G}_4(R_h(t_j), t_j)}{\Gamma(\xi+2)} \\
&\times\Delta^{\xi}\Big[(j+1-i)^{\xi}(j-i+2+\xi) - (j-i)^{\xi}(j-i+2+2\xi)\Big] \\
&-\frac{\mathbf{G}_4(R_h(t_{j-1}), t_{j-1})}{\xi(\xi+2)}\Delta^{\xi}[(j+1-i)^{\xi+1} - (j-i)^{\xi}(j-i+1+\xi)]\Big), \qquad (4.9)
\end{aligned}$$

$$\begin{aligned}
S_d(t_{j+1}) &= S_d(t_0) + \frac{(1-\xi)}{M(\xi)}\Big[\mathbf{G}_5(S_d(t_j), t_j)\Big] + \frac{\xi}{M(\xi)}\sum_{i=0}^{j}\Big(\frac{\mathbf{G}_5(S_d(t_j), t_j)}{\Gamma(\xi+2)} \\
&\times\Delta^{\xi}\Big[(j+1-i)^{\xi}(j-i+2+\xi) - (j-i)^{\xi}(j-i+2+2\xi)\Big] \\
&-\frac{\mathbf{G}_5(S_d(t_{j-1}), t_{j-1})}{\xi(\xi+2)}\Delta^{\xi}[(j+1-i)^{\xi+1} - (j-i)^{\xi}(j-i+1+\xi)]\Big), \qquad (4.10)\\
E_d(t_{j+1}) &= E_d(t_0) + \frac{(1-\xi)}{M(\xi)}\Big[\mathbf{G}_6(E_d(t_j), t_j)\Big] + \frac{\xi}{M(\xi)}\sum_{i=0}^{j}\Big(\frac{\mathbf{G}_6(E_d(t_j), t_j)}{\Gamma(\xi+2)} \\
&\times\Delta^{\xi}\Big[(j+1-i)^{\xi}(j-i+2+\xi) - (j-i)^{\xi}(j-i+2+2\xi)\Big] \\
&-\frac{\mathbf{G}_6(E_d(t_{j-1}), t_{j-1})}{\xi(\xi+2)}\Delta^{\xi}[(j+1-i)^{\xi+1} - (j-i)^{\xi}(j-i+1+\xi)]\Big), \qquad (4.11)
\end{aligned}$$

$$
\begin{aligned}
I_d(t_{j+1}) &= I_d(t_0) + \frac{(1-\xi)}{M(\xi)}\Big[\mathbf{G}_7(I_d(t_j), t_j)\Big] + \frac{\xi}{M(\xi)}\sum_{i=0}^{j}\Big(\frac{\mathbf{G}_7(I_d(t_j), t_j)}{\Gamma(\xi+2)} \\
&\times\Delta^{\xi}\Big[(j+1-i)^{\xi}(j-i+2+\xi) - (j-i)^{\xi}(j-i+2+2\xi)\Big] \\
&-\frac{\mathbf{G}_7(I_d(t_{j-1}), t_{j-1})}{\xi(\xi+2)}\Delta^{\xi}[(j+1-i)^{\xi+1} - (j-i)^{\xi}(j-i+1+\xi)]\Big), \qquad (4.12)\\
V_d(t_{j+1}) &= V_d(t_0) + \frac{(1-\xi)}{M(\xi)}\Big[\mathbf{G}_8(V_d(t_j), t_j)\Big] + \frac{\xi}{M(\xi)}\sum_{i=0}^{j}\Big(\frac{\mathbf{G}_8(V_d(t_j), t_j)}{\Gamma(\xi+2)} \\
&\times\Delta^{\xi}\Big[(j+1-i)^{\xi}(j-i+2+\xi) - (j-i)^{\xi}(j-i+2+2\xi)\Big] \\
&-\frac{\mathbf{G}_8(E_d(t_{j-1}), t_{j-1})}{\xi(\xi+2)}\Delta^{\xi}[(j+1-i)^{\xi+1} - (j-i)^{\xi}(j-i+1+\xi)]\Big), \qquad (4.13)
\end{aligned}
$$

4.1. Numerical simulation results of the model and discussion

This section presents graphical results from numerical simulations, evaluating the model's outcomes across varying fractional-order levels. The findings are analyzed against the dataset presented in Table 2 as shown in Figure 3, applying the defined initial conditions [23].

Table 2. Parameters and their numerical values in the model (2.5).

Notation	Value	Source	Notation	Value	Source
Λ_h	2000	Assumed	Λ_d	500	Assumed
μ_h	0.0022	[24]	μ_d	0.83	[24]
σ_h	0.004	[24]	σ_d	0.0002	[24]
ρ_h	0.71	[25]	ρ_d	0.31	[25]
φ_h	0.29	[25]	φ_d	0.17	[25]
ω_h	0.19	[25]	ω_d	0.005	[25]
S_h	430	Assumed	E_h	40	Assumed
I_h	20	Assumed	R_h	0	Assumed
S_d	230	Assumed	E_d	60	Assumed
I_d	10	Assumed	V_d	0	Assumed
β_d	0.29	Global Alliance	β_{h1}	0.304	Global Alliance
β_{h2}	0.58	Global Alliance			

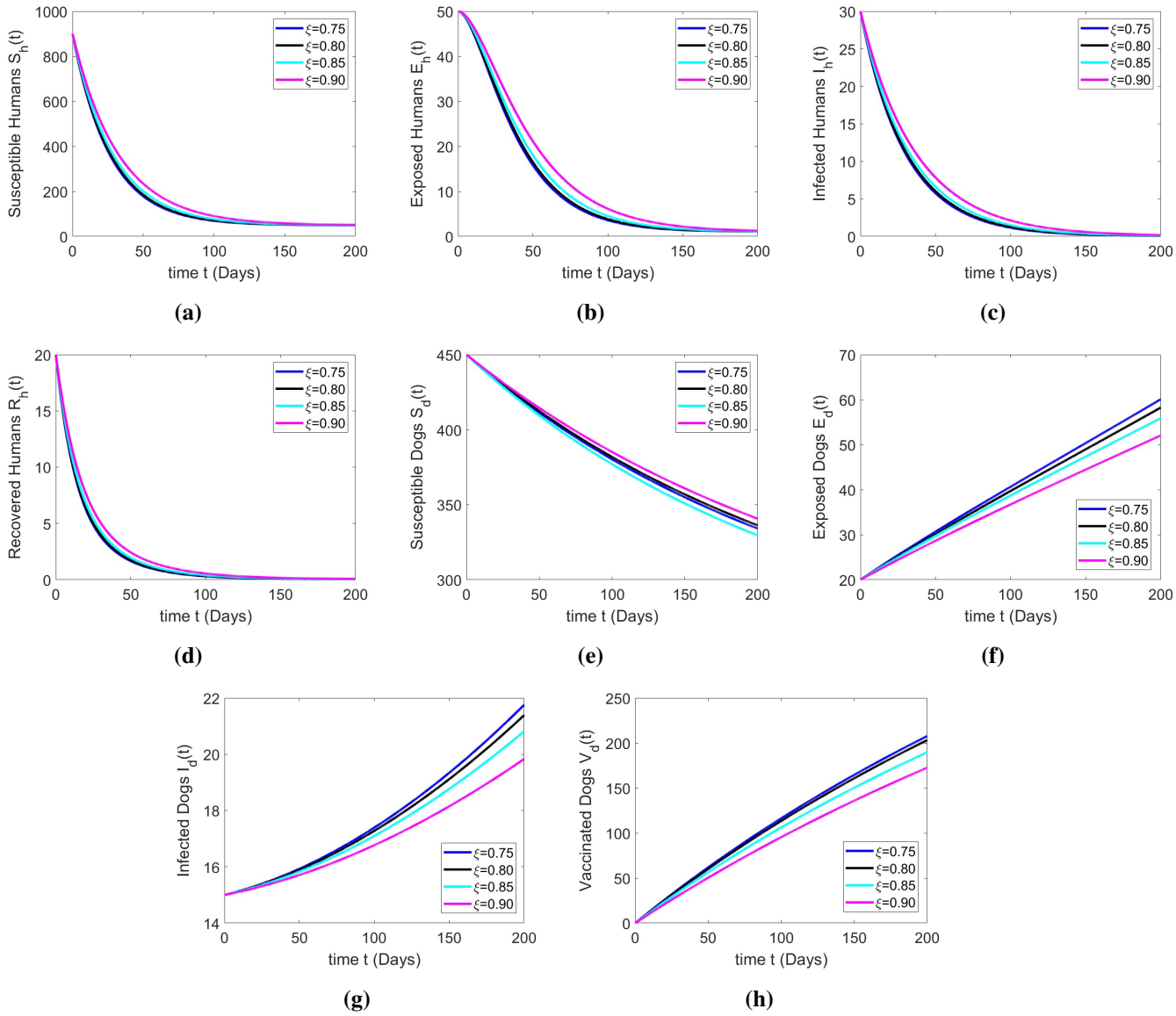

Figure 3. The numerical simulation graphs representing the susceptible, exposed, infected, and recovered Humans; susceptible, exposed, infected, and vaccinated dogs.

To ensure reliable predictive performance, the DNN architecture was carefully designed, comprising three hidden layers with 10, 100, and 10 neurons, respectively. This configuration provided an optimal balance between model complexity and generalization, consistent with approaches in recent studies on fractional epidemiological models. Sigmoid activation functions were applied in the hidden layers to capture nonlinear relationships, while a linear activation function was employed in the output layer to accommodate regression-based predictions. A log-sigmoid activation function was employed in the hidden layers due to its suitability for modeling nonlinear epidemiological dynamics. While this choice ensured convergence, alternative activation functions such as Rectified Linear Unit (ReLU), Exponential Linear Unit (ELU), and hyperbolic tangent (tanh) could potentially enhance learning efficiency. This limitation will be addressed in future studies by benchmarking multiple activation strategies. The Levenberg-Marquardt optimization algorithm was

selected for its efficiency in achieving rapid convergence on medium-scale datasets. Alternative optimization techniques such as Adam, Root Mean Square Propagation (RMSProp), and stochastic gradient descent (SGD) were not implemented in this study but will be explored in future work for scalability and performance comparison. The dataset was partitioned into training, validation, and testing subsets with proportions of 70%, 15%, and 15%, respectively, following standard supervised learning practices. The network was trained over 1000 epochs. Hyperparameters such as learning rate, batch size, and early stopping criteria were optimized to enhance performance and prevent overfitting. The computational complexity of the proposed DNN architecture was primarily influenced by the number of hidden neurons (10–100–10) and training epochs (1000). The overall complexity can be approximated as $O(n \times m \times L)$, where n is the number of neurons, m is the size of the training data, and L is the number of layers. While this deep structure offers improved predictive power, it introduces a higher computational burden compared with shallow architectures, which remains a trade-off between accuracy and efficiency. Future work will explore lightweight architectures to optimize complexity without sacrificing performance. The architecture of this model in the sense of a neural network is given as Figure 4.

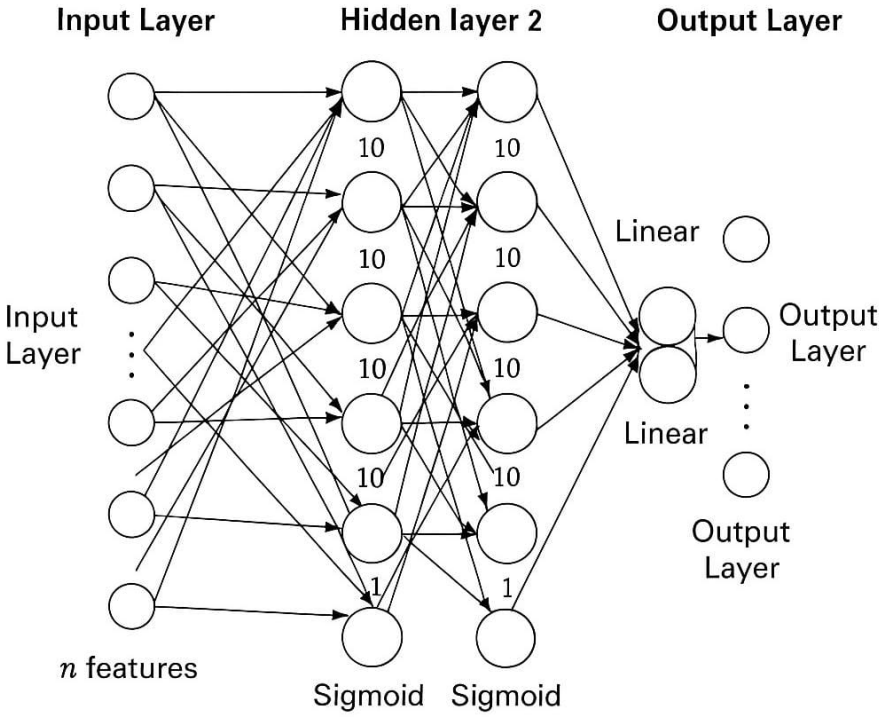

Figure 4. The deep neural network's architecture.

Model evaluation was conducted using multiple statistical indicators, including the mean squared error (MSE), root mean squared error (RMSE), and the coefficient of determination (R^2), ensuring robustness and accuracy of predictions across compartments. Residual plots were generated to assess prediction errors, and uncertainty bands were included where applicable to indicate confidence intervals around the model's predictions. Time-series overlays comparing predicted and observed dynamics demonstrated strong concordance throughout the simulation period. To complement the

DNN training, the fractional Adams-Bashforth method was implemented to numerically approximate the solutions of the fractional differential equations. This hybrid approach ensured consistency between the mechanistic and data-driven frameworks, significantly enhancing the model's analytical and predictive capabilities. Regression analyses confirmed the stability and convergence, highlighting the synergy between fractional calculus and deep learning.

To provide intuitive insights into the model's performance, we include several visual diagnostics. Time-series overlays compare predicted and observed case counts for key epidemiological compartments, illustrating strong concordance over the simulation period. Residual plots highlight the distribution and magnitude of prediction errors, confirming the model's reliability and pinpointing areas for refinement. Where applicable, uncertainty bands are displayed to indicate confidence intervals around the model's predictions. All figures have been enhanced to meet or exceed 300 dpi resolution standards, with enlarged axis labels and legends to ensure readability in print and electronic formats. Furthermore, a schematic graphic summarizing the data flow, neural network pipeline, and epidemiological outputs has been added to facilitate understanding of the integrated methodology.

Figure 5a illustrates the data for the $S_h(t)$ class, analyzed using DNN. The regression coefficient is approximately one, with a MSE of $1.4635e-06$ and a RMSE of 0.0021127. The histogram shows mean (ME) and variance errors (VE) of $2.3855e-05$ and 0.0021127, validating the proposed method. Figure 5b presents the training data for $S_h(t)$, achieving regression near one, with a MSE and RMSE of $4.3731e-06$ and 0.0020912, respectively. Histogram analysis shows a ME and VE of $6.6871e-06$ and 0.0020914, confirming the method's reliability. The testing results for $S_h(t)$, shown in Figure 6c, yield a regression coefficient close to one, with a MSE of $1.5602e-06$ and a RMSE of 0.0021355. The histogram analysis indicates ME and VE of -0.00016368 and 0.16293, further supporting the model's accuracy. Validation data for $S_h(t)$, shown in Figure 5d, report a regression coefficient of one, with a MSE and RMSE of $1.7888e-06$ and 0.0021883, respectively. Histogram analysis reveals a ME and VE of $8.6248e-05$ and 0.0021877, reinforcing the method's validity. A comparison plot for $S_h(t)$ using the DNN is displayed in Figure 5e, while Figure 5f highlights the absolute inaccuracies (AE).

Figure 6a illustrates the data for the $E_h(t)$ class, analyzed using DNN. The regression coefficient is approximately one, with a MSE of $1.2784e-08$ and a RMSE of 0.00011307. The histogram shows a ME and VE of $-3.7274e-07$ and 0.00011308, validating the proposed method. Figure 6b presents the training data for $E_h(t)$, achieving regression near one, with a ME and RMSE of $1.478e-08$ and 0.00012157, respectively. Histogram analysis shows ME and VE of $-1.1669e-07$ and 0.00012159, confirming the method's reliability. The testing results for $E_h(t)$, shown in Figure 6c, yield a regression coefficient close to one, with a MSE of $5.7058e-09$ and a RMSE of $7.5537e-05$. The histogram analysis indicates a ME and VE of $-1.4091e-07$ and $7.5575e-05$, further supporting the model's accuracy. Validation data for $E_h(t)$, shown in Figure 6d, report a regression coefficient of one, with a MSE and RMSE of $1.055e-08$ and 0.00010271, respectively. Histogram analysis reveals a ME and VE of $-1.7995e-06$ and 0.00010275, reinforcing the method's validity. A comparison plot for $E_h(t)$ using the DNN is displayed in Figure 6e, while Figure 6f highlights the absolute inaccuracies.

Figure 7a presents the data for the $I_h(t)$ class, analyzed using a DNN. The regression coefficient in this case is approximately one, with a MSE of $5.9402e-09$ and a RMSE of $7.7073e-05$. Histogram analysis reveals a ME and VE of $-6.8072e-07$ and $7.7076e-05$, confirming the accuracy of the proposed method. Figure 7b illustrates the training data for $I_h(t)$, processed through the DNN. For this scenario, the regression coefficient is close to one, with a MSE and RMSE of $5.8535e-09$ and

$7.6508e-05$, respectively. The histogram shows a ME and VE of $-3.6809e-07$ and $7.6516e-05$, validating the reliability of the method. For the $I_h(t)$ class, as shown in Figure 7c, the regression coefficient remains around one, with a MSE of $6.004e-09$ and a RMSE of $7.7486e-05$. The histogram depicts ME and VE of $-2.1161e-06$ and $7.7495e-05$, confirming the accuracy of the approach. Similarly, Figure 7d presents the validation data for $I_h(t)$, where the regression coefficient is one. The MSE is $6.2809e-09$, and the RMSE is $7.9252e-05$. Histogram analysis reveals a ME and VE of $-7.0436e-07$ and $7.9289e-05$, further supporting the correctness of the proposed technique. The comparison plot for $I_h(t)$ using the DNN is displayed in Figure 7e, while Figure 7f highlights the absolute inaccuracies.

Figure 8a presents the results for all points of the $R_h(t)$ class. The regression coefficient is 1, with a MSE and RMSE of $9.8356e-08$ and 0.00031362. The histogram demonstrates a ME and VE of $2.7219e-06$ and 0.00031363, validating the accuracy of the proposed method. Figure 8b shows the training data for the $R_h(t)$ class analyzed using the DNN. The regression coefficient is 1, with a MSE of $9.582e-08$ and RMSE of 0.00030955. The histogram highlights a ME and VE of $2.0197e-07$ and 0.00030958, confirming the effectiveness of the technique. The regression coefficient for the $R_h(t)$ class remains close to 1, as depicted in Figure 8c. The MSE is $1.0499e-07$, and the RMSE is 0.00032403. The histogram illustrates a ME and VE of $-4.3186e-06$ and 0.00032416, respectively, further validating the accuracy of the suggested approach. Similarly, Figure 8d displays the validation data for the $R_h(t)$ class, processed using the DNN. The regression coefficient is 1, with an MSE of $1.0355e-07$ and a RMSE of 0.0003218. The histogram shows a ME and VE of $2.1523e-05$ and 0.00032124, supporting the correctness of the proposed method. A comparison plot for $R_h(t)$ using the DNN is provided in Figure 8e, while Figure 8f highlights the absolute inaccuracies.

Figure 9a illustrates the data for the $S_d(t)$ class, analyzed using a DNN. The regression coefficient is approximately one, with a MSE of $3.4142e-10$ and a RMSE of 1.8478e-05. The histogram shows a ME and VE of $1.8805e-07$ and $1.8478e-05$, validating the proposed method. Figure 9b presents the training data for $S_d(t)$, achieving regression near one, with a ME and RMSE of $3.334e-10$ and $1.8259e-05$, respectively. Histogram analysis shows a ME and VE of $-5.8788e-08$ and $1.8261e-05$, confirming the method's reliability. The testing results for $S_d(t)$, shown in Figure 9c, yield a regression coefficient close to one, with a MSE of $3.6325e-10$ and a RMSE of $1.9059e-05$. The histogram analysis indicates a ME and VE of $9.2962e-07$ and $1.9046e-05$, further supporting the model's accuracy. Validation data for $S_d(t)$, shown in Figure 9d, report a regression coefficient of one, with a MSE and RMSE of $3.5703e-10$ and $1.8895e-05$, respectively. Histogram analysis reveals a ME and VE of $5.9849e-07$ and $1.8895e-05$, reinforcing the method's validity. A comparison plot for $S_d(t)$ using the DNN is displayed in Figure 9e, while Figure 9f highlights the absolute inaccuracies.

Figure 10a presents the data for the $E_d(t)$ class, analyzed using a DNN. The regression coefficient in this case is approximately one, with a MSE of $8.252e-10$ and a RMSE of $2.8726e-05$. Histogram analysis a ME and VE of $7.8965e-08$ and $2.8728e-05$, confirming the accuracy of the proposed method. Figure 10b illustrates the training data for $E_d(t)$, processed through the DNN. For this scenario, the regression coefficient is close to one, with a MSE and RMSEs of $8.1647e-10$ and $2.8574e-05$, respectively. The histogram shows a ME and VE of $-8.7563e-10$ and $2.8577e-05$, validating the reliability of the method. For the $E_d(t)$ class, as shown in Figure 10c, the regression coefficient remains around one, with a MSE of $8.4308e-10$ and a RMSE of $2.9036e-05$. The histogram depicts a ME and VE of $-1.0917e-06$ and $2.903e-05$, confirming the accuracy of the approach. Similarly,

Figure 10d presents the validation data for $E_d(t)$, where the regression coefficient is one. The MSE is $8.4808e-10$, and the RMSE is $2.9122e-05$. Histogram analysis reveals a ME and VE of $1.6223e-06$ and $2.9091e-05$, further supporting the correctness of the proposed technique. The comparison plot for $E_d(t)$ using the DNN is displayed in Figure 10e, while Figure 10f highlights the absolute inaccuracies.

Figure 11a presents the results for all points of the $I_d(t)$ class. The regression coefficient is 1, with a MSE and RMSE of $3.1066e-12$ and $1.7626e-06$. The histogram demonstrates a ME and VE of $-1.1388e-08$ and $1.7627e-06$, validating the accuracy of the proposed method. Figure 11b shows the training data for the $I_d(t)$ class analyzed using the DNN. The regression coefficient is 1, with an MSE of $3.0362e-12$ and a RMSE of $1.7425e-06$. The histogram highlights a ME and VE of $-1.5238e-09$ and $1.7426e-06$, confirming the effectiveness of the technique. The regression coefficient for the $I_d(t)$ class remains close to 1, as depicted in Figure 11c. The MSE is $3.2648e-12$, and the RMSE is $1.8069e-06$. The histogram illustrates a ME and VE of $2.7848e-08$ and $1.8076e-06$, respectively, further validating the accuracy of the suggested approach. Similarly, Figure 11d displays the validation data for the $I_d(t)$ class, processed using the DNN. The regression coefficient is 1, with a MSE of $3.2773e-12$ and a RMSE of $1.8103e-06$. The histogram shows a ME and VE of $-9.6658e-08$ and $1.8086e-06$, supporting the correctness of the proposed method. A comparison plot for $I_d(t)$ using the DNN is provided in Figure 11e, while Figure 11f highlights the absolute inaccuracies.

Figure 12a presents the results for all points of the $V_d(t)$ class. The regression coefficient is 1, with a MSE and RMSE of $2.2454-09$ and $4.7386e-05$. The histogram demonstrates a ME and VE of $-1.495e-07$ and $4.7389e-05$, validating the accuracy of the proposed method. Figure 12b shows the training data for the $V_d(t)$ class analyzed using the DNN. The regression coefficient is 1, with an MSE of $2.2119e-09$ and RMSE of $4.7031e-05$. The histogram highlights a ME and VE of $6.0275e-08$ and $4.7036e-05$, confirming the effectiveness of the technique. The regression coefficient for the $V_d(t)$ class remains close to 1, as depicted in Figure 12c. The MSE is $2.2635e-09$, and the RMSE is $4.7576e-05$. The histogram illustrates a ME and VE of $-7.2754e-07$ and $4.7594e-05$, respectively, further validating the accuracy of the suggested approach. Similarly, Figure 12d displays the validation data for the $V_d(t)$ class, processed using the DNN. The regression coefficient is 1, with a MSE of $2.3838e-09$ and a RMSE of $4.8824e-05$. The histogram shows a ME and VE of $-5.5045e-07$ and $4.8846e-05$, supporting the correctness of the proposed method. A comparison plot for $V_d(t)$ using the DNN is provided in Figure 12e, while Figure 12f highlights the absolute inaccuracies.

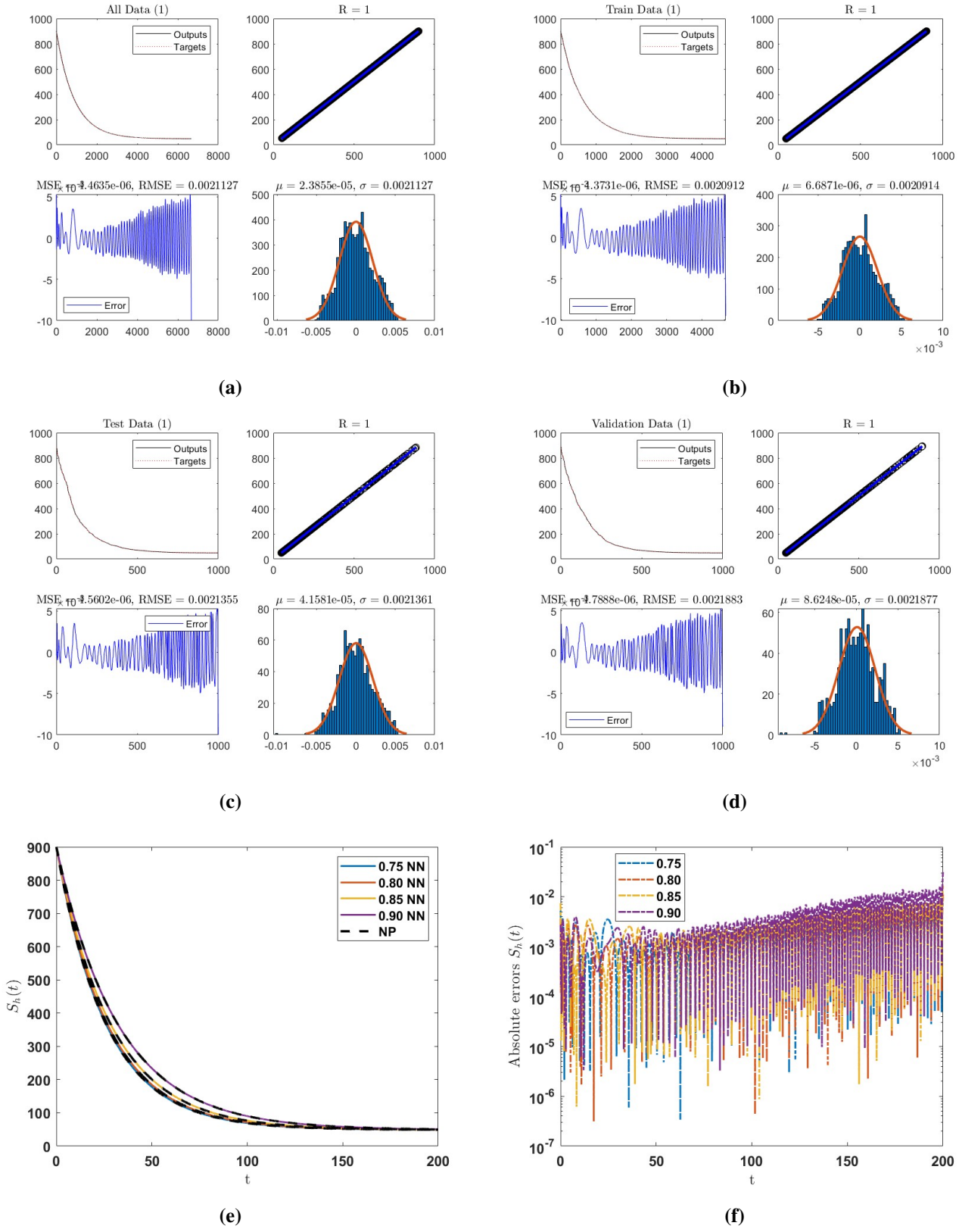

Figure 5. Dynamical behavior for class $S_h(t)$ with the DNN: (a) all points, (b) training points, (c) testing points, (d) points of validation, (e) the comparison plot, and (f) the AE.

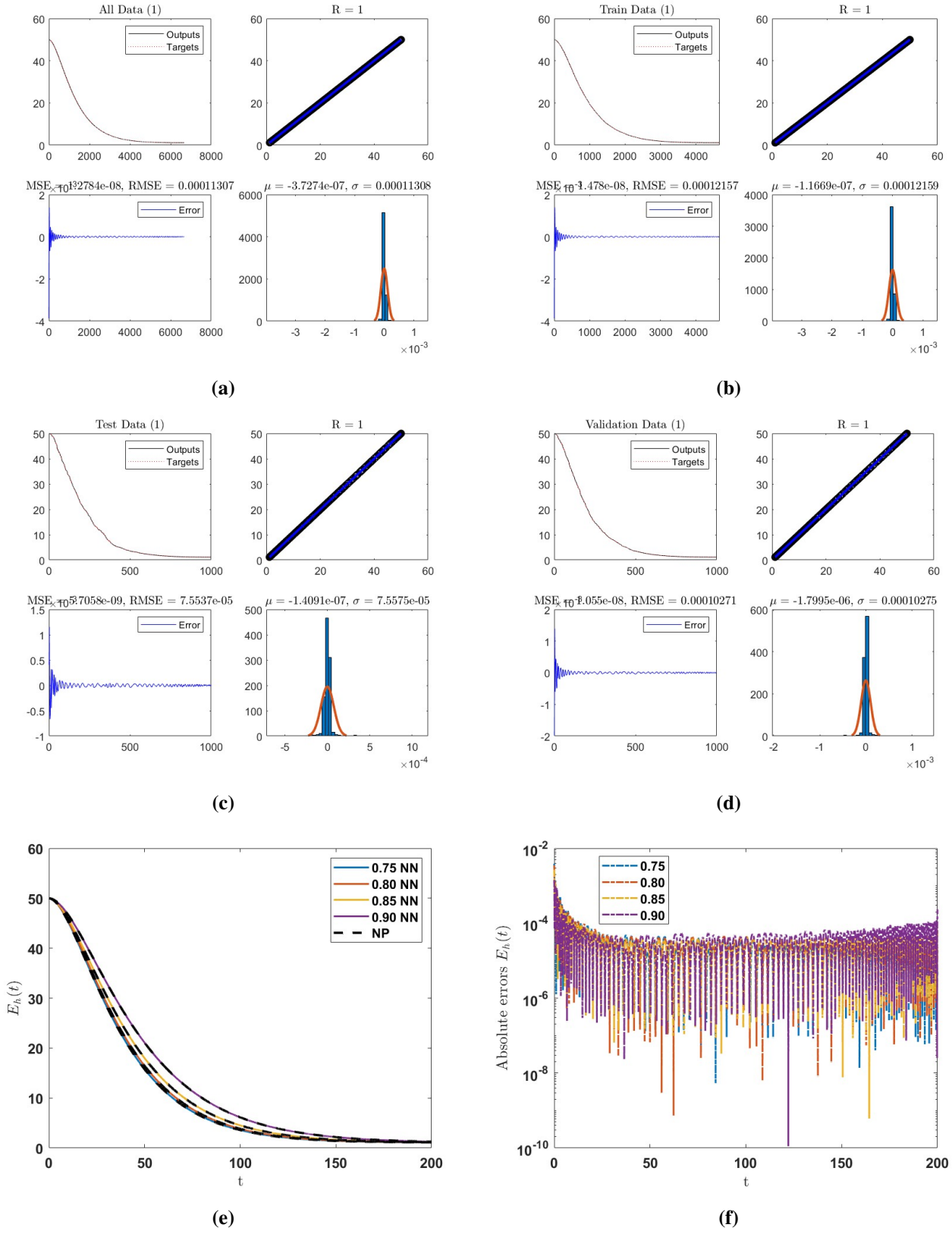

Figure 6. Dynamical behavior for class $E_h(t)$ with the DNN: (a) all points, (b) training points, (c) testing points, (d) points of validation, (e) the comparison plot, and (f) the AE.

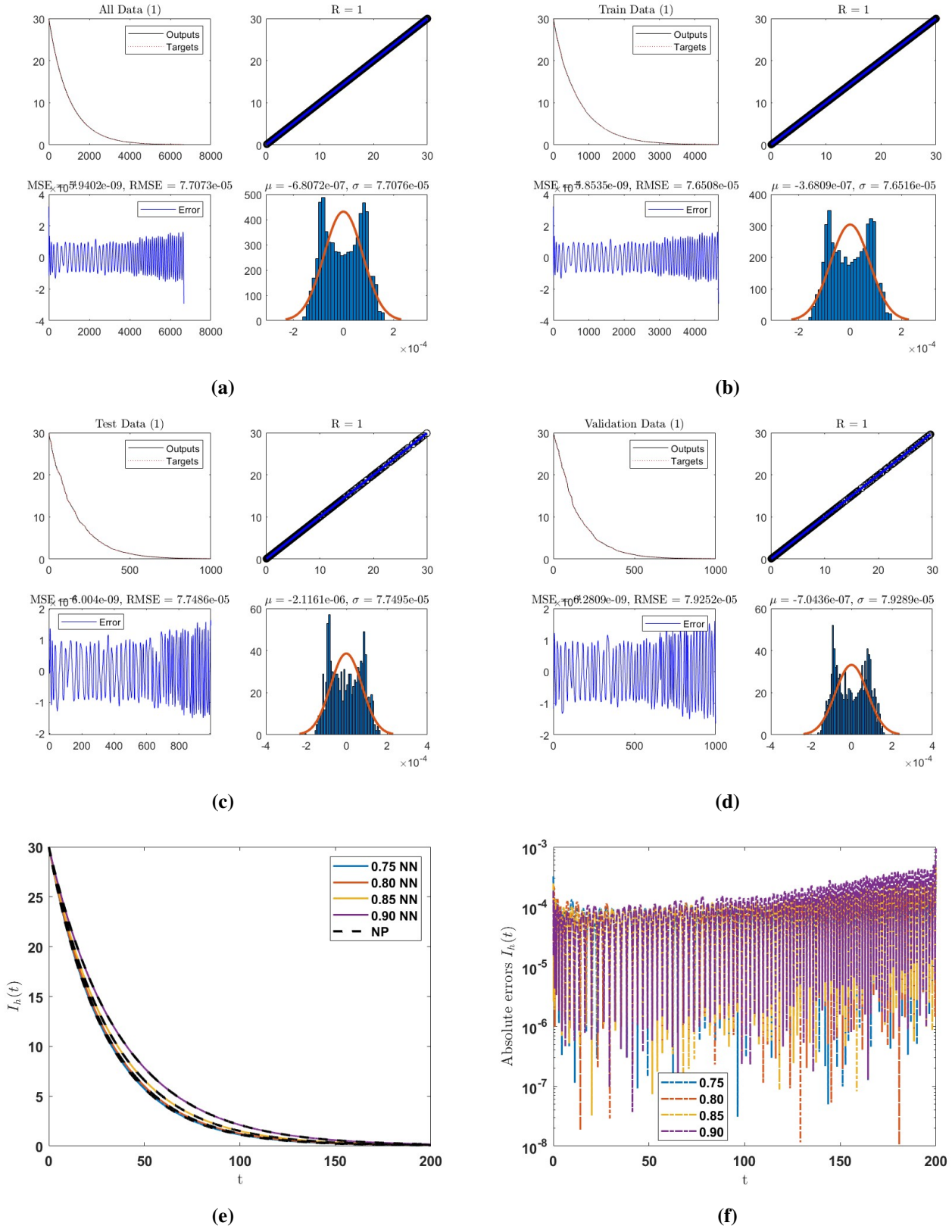

Figure 7. Dynamical behavior for class $I_h(t)$ with the DNN: (a) all points, (b) training points, (c) testing points, (d) points of validation, (e) the comparison plot, and (f) the AE.

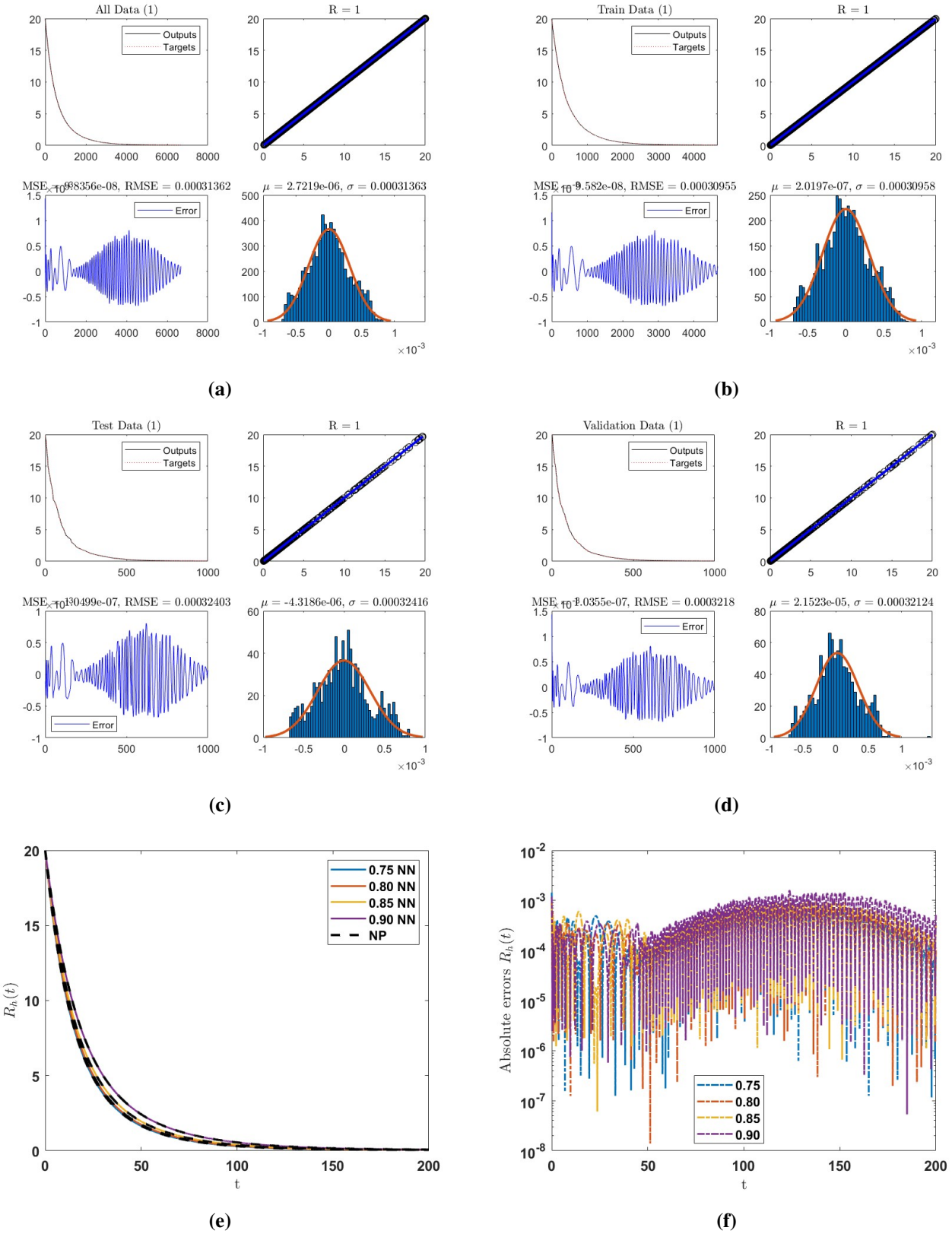

Figure 8. Dynamical behavior for class $R_h(t)$ with the DNN: (a) all points, (b) training points, (c) testing points, (d) points of validation, (e) the comparison plot, and (f) the AE.

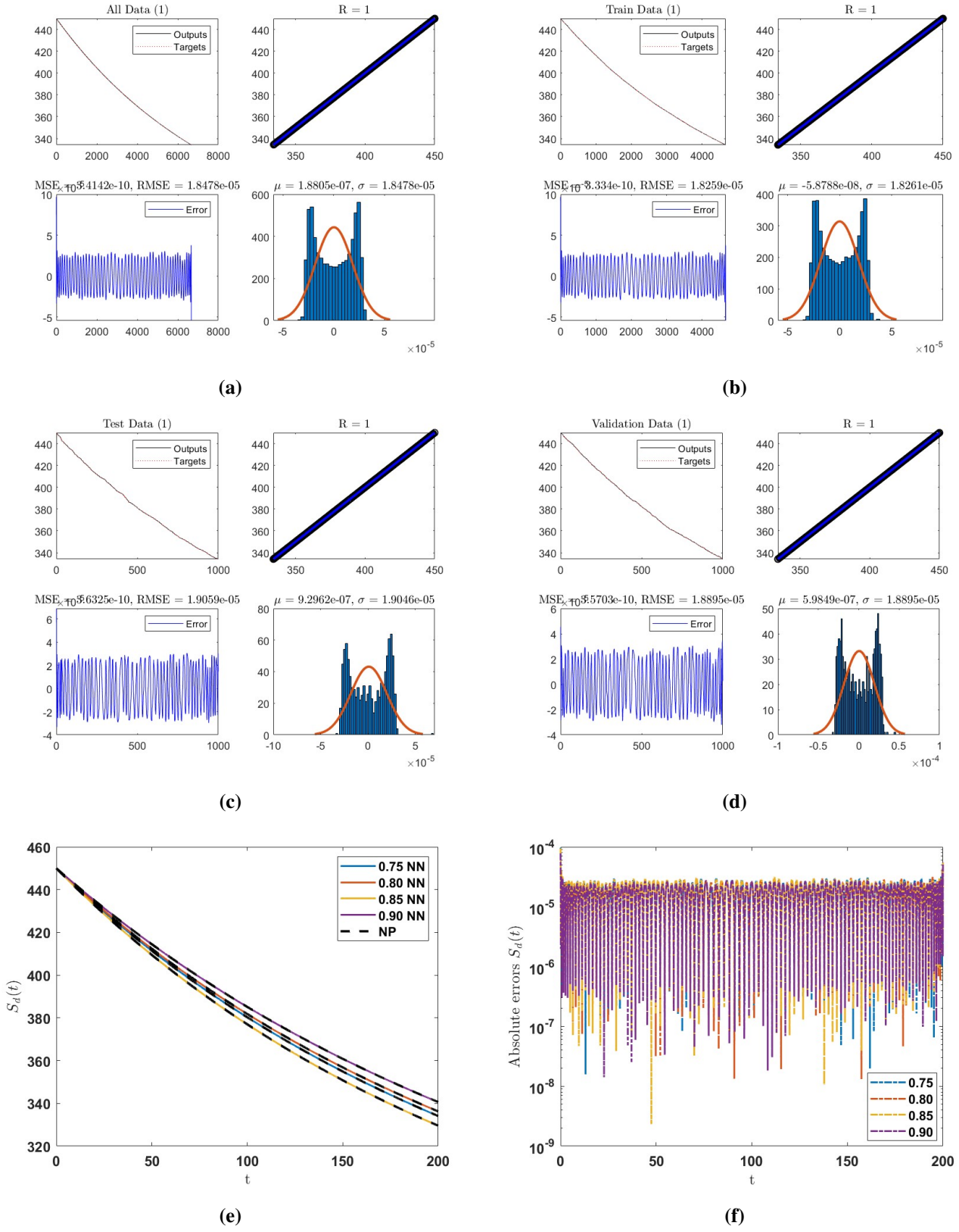

Figure 9. Dynamical behavior for class $S_d(t)$ with the DNN: (a) all points, (b) training points, (c) testing points, (d) points of validation, (e) the comparison plot, and (f) the AE.

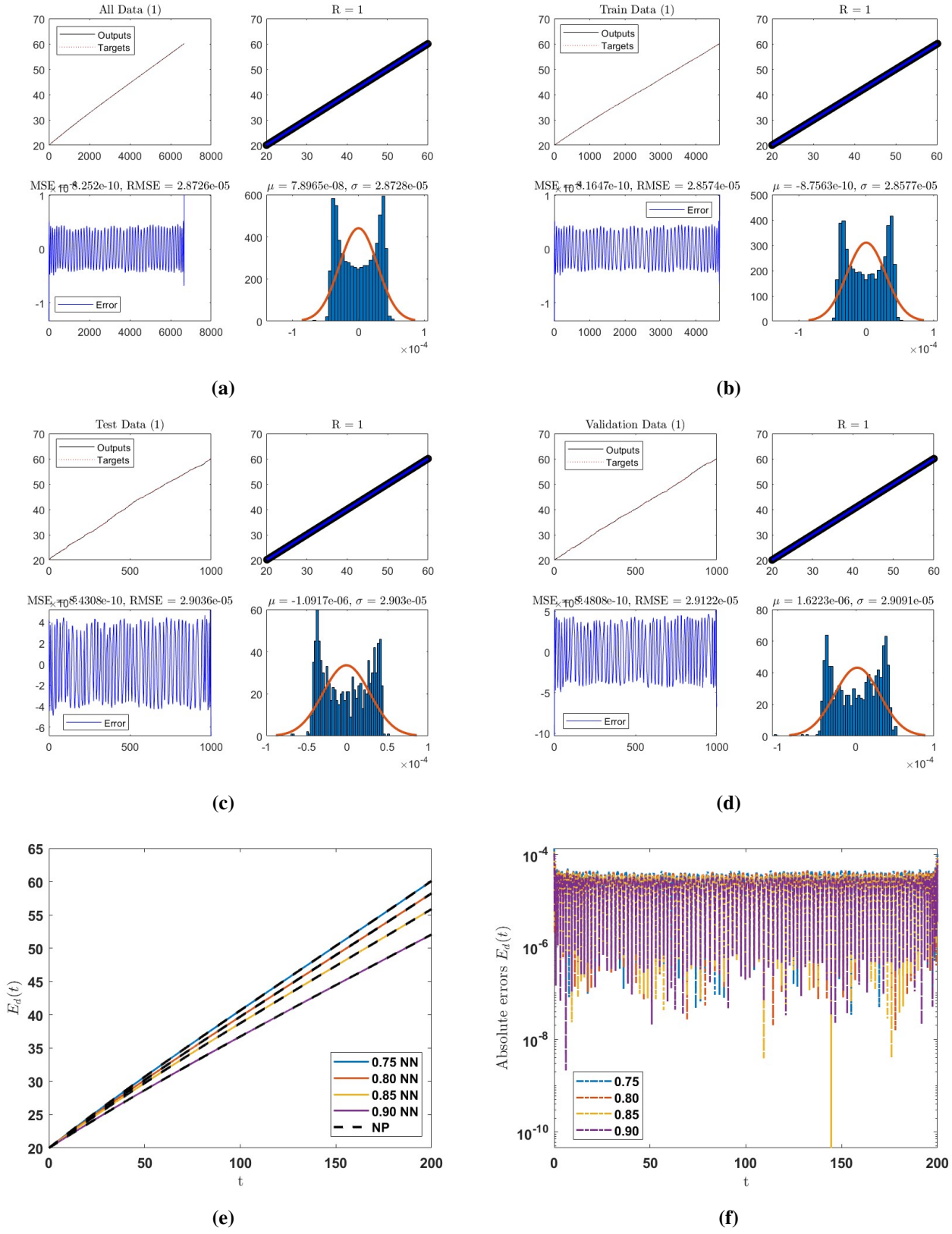

Figure 10. Dynamical behavior for class $E_d(t)$ with the DNN: (a) all points, (b) training points, (c) testing points, (d) points of validation, (e) the comparison plot, and (f) the AE.

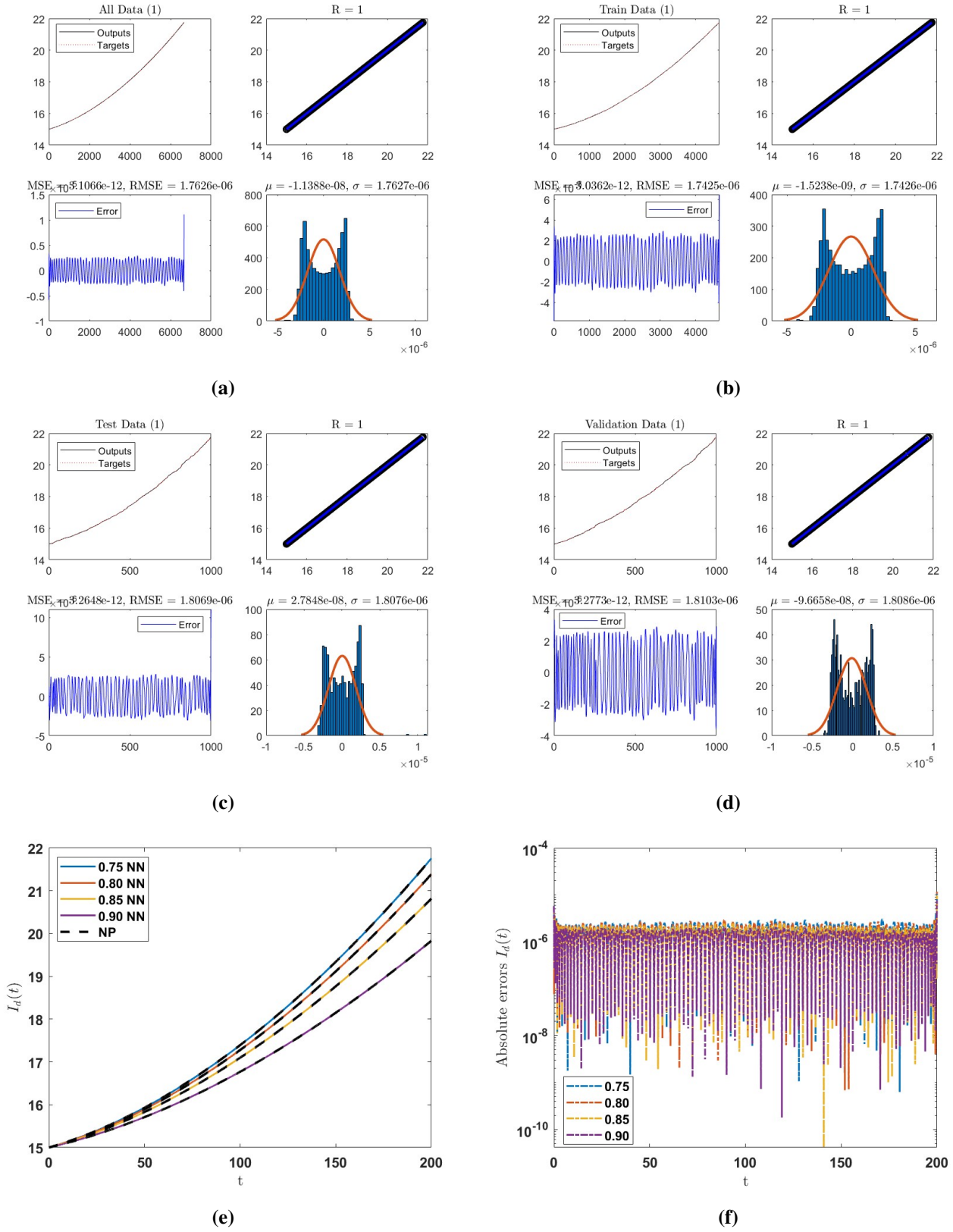

Figure 11. Dynamical behavior for class $I_d(t)$ with the DNN: (a) all points, (b) training points, (c) testing points, (d) points of validation, (e) the comparison plot, and (f) the AE.

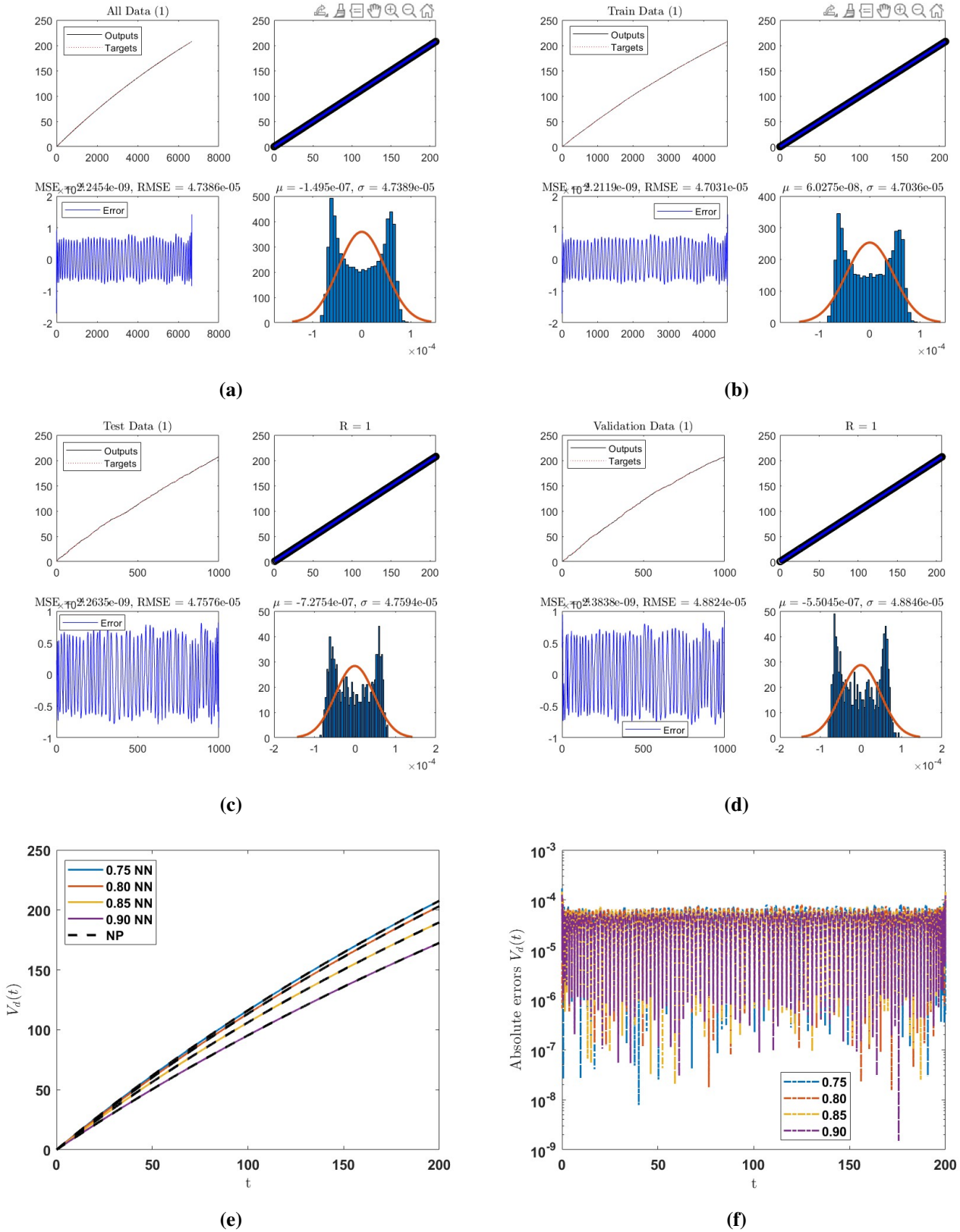

Figure 12. Dynamical behavior for class $V_d(t)$ with the DNN: (a) all points, (b) training points, (c) testing points, (d) points of validation, (e) the comparison plot, and (f) the AE.

5. Conclusions

This manuscript presents an in-depth exploration of rabies transmission dynamics in human and dog populations through an eight-compartment model employing the generalized ABC fractional operator. The study validates the dynamic behavior of each compartment across varying fractional orders, demonstrating the flexibility and robustness of derivative selection within this framework. Using fixed-point theory, the existence and uniqueness of the solutions are established in a generalized context, while a stability analysis is conducted via the Ulam-Hyers approach. Numerical simulations are facilitated by the Adams-Bashforth method, enabling approximate solutions over varying fractional orders, iterative time intervals, and diverse initial conditions. For smaller fractional orders, the model exhibits higher precision and stability, whereas larger fractional orders yield amplified effects and more complex behavior. Additionally, comparisons with the Laplace-Adomian decomposition method underscore the applicability of the numerical approach to both fractional and classical models. DNN techniques were employed to partition the dataset into training, testing, and validation subsets, allowing detailed analysis of the data's characteristics and patterns. This integration of fractional differential equations with DNNs establishes a practical framework to model complex disease transmission dynamics, highlighting the critical role of vaccination in controlling rabies spread. The limitations of the current work include assumptions of homogeneous mixing and the exclusion of specific transmission pathways, which merit further investigation. Future research directions include extending the model to incorporate more generalized fractional operators, adapting the framework for multi-strain rabies, applying transfer learning to other zoonotic diseases, and incorporating physics-informed neural network loss functions to enhance interpretability and predictive power. These advances underscore the broad potential of this approach to inform and improve public health interventions targeting rabies and related infectious diseases. Future work will integrate modern heuristic algorithms (e.g., genetic algorithms, particle swarm optimization, grey wolf optimizer) to optimize hyperparameters such as the learning rate, neuron allocation, and regularization parameters. These approaches have demonstrated significant potential in improving training efficiency and prediction accuracy in similar modeling frameworks.

Author contributions

All authors contributed to the study. Specifically, R. Shafqat conceptualized the study; M. Z. Meetei designed the methodology; A. H. Msmali was responsible for software; W. Hamali was responsible for formal analysis; R. Shafqat was responsible for the investigation of the study; R. Shafqat and M. Z. Meetei was responsible for the resources; R. Shafqat, A. H. Msmali and W. Hamali wrote the original draft; R. Shafqat and M. Z. Meetei were responsible for reviewing and editing; R. Shafqat supervised the study; A. H. Msmali and W. Hamali were responsible for project administration; M. Z. Meetei was responsible for funding acquisition. All authors have read and approved the final version of the manuscript for publication.

Use of Generative-AI tools declaration

The authors declare they have not used Artificial Intelligence (AI) tools in the creation of this article.

Acknowledgments

The authors gratefully acknowledge the funding of the Deanship of Graduate Studies and Scientific Research, Jazan University, Saudi Arabia, through project number JU-202502109-DGSSR-RP-2025.

Conflict of interest

All authors declare no conflicts of interest in this paper.

References

1. K. M. Addo, *An SEIR mathematical model for dog rabies; Case study: Bongo District, Ghana*, Doctoral dissertation, 2012.
2. Q. Hou, Z. Jin, S. Ruan, Dynamics of rabies epidemics and the impact of control efforts in Guangdong Province, China, *J. Theor. Biol.*, **300** (2012), 39–47. https://doi.org/10.1016/j.jtbi.2012.01.006
3. R. M. Anderson, H. C. Jackson, R. M. May, A. M. Smith, Population dynamics of fox rabies in Europe, *Nature*, **289** (1981), 765–771. https://doi.org/10.1038/289765a0
4. D. L. Smith, B. Lucey, L. A. Waller, J. E. Childs, L. A. Real, Predicting the spatial dynamics of rabies epidemics on heterogeneous landscapes, *P. Natl. Acad. Sci.*, **99** (2002), 3668–3672. https://doi.org/10.1073/pnas.042400799
5. C. A. Russell, D. L. Smith, J. E. Childs, L. A. Real, Predictive spatial dynamics and strategic planning for raccoon rabies emergence in Ohio, *PLoS Biol.*, **3** (2005), e88. https://doi.org/10.1371/journal.pbio.0030088 ’
6. E. Asano, L. J. Gross, S. Lenhart, L. A. Real, Optimal control of vaccine distribution in a rabies metapopulation model, *Math. Biosci. Eng.*, **5** (2008), 219–238. https://doi.org/10.3934/mbe.2008.5.219
7. J. Zhang, Z. Jin, G. Q. Sun, T. Zhou, S. Ruan, Analysis of rabies in China: Transmission dynamics and control, *PLoS One*, **6** (2011), e20891. https://doi.org/10.1371/journal.pone.0020891
8. O. C. Eze, G. E. Mbah, D. U. Nnaji, N. E. Onyiaji, Mathematical modelling of transmission dynamics of rabies virus, *Int. J. Math. Trends Technol.-IJMTT*, **66** (2020). https://doi.org/10.14445/22315373/IJMTT-V66I7P506
9. T. T. Ega, L. Luboobi, D. Kuznetsov, Modeling the dynamics of rabies transmission with vaccination and stability analysis, *Appl. Comput. Math.*, **4** (2015). https://doi.org/10.11648/j.acm.20150406.13
10. M. Sambo, S. Cleaveland, H. Ferguson, T. Lembo, C. Simon, H. Urassa, et al., The burden of rabies in Tanzania and its impact on local communities, *PLoS Neglect. Trop. D.*, **7** (2013), e2510. https://doi.org/10.1371/journal.pntd.0002510
11. S. Ruan, Modeling the transmission dynamics and control of rabies in China, *Math. Biosci.*, **286** (2017), 65–93. https://doi.org/10.1016/j.mbs.2017.02.005
12. M. Laager, *Mathematical modelling of dog rabies transmission in N’Djamena, Chad*, Doctoral dissertation, University of Basel, 2018.

13. A. Atangana, K. M. Owolabi, New numerical approach for fractional differential equations, *Math. Model. Nat. Phenom.*, **13** (2018), 3. https://doi.org/10.1051/mmnp/2018010
14. R. Shafqat, A. Alsaadi, Artificial neural networks for stability analysis and simulation of delayed rabies spread models, *AIMS Math.*, **9** (2024), 33495–33531. https://doi.org/10.3934/math.20241599
15. A. Turab, R. Shafqat, S. Muhammad, M. Shuaib, M. F. Khan, M. Kamal, Predictive modeling of hepatitis B viral dynamics: A Caputo derivative-based approach using artificial neural networks, *Sci. Rep.*, **14** (2024), 21853. https://doi.org/10.1038/s41598-024-70788-7
16. K. Abuasbeh, R. Shafqat, A. Alsinai, M. Awadalla, Analysis of the mathematical modelling of COVID-19 by using mild solution with delay Caputo operator, *Symmetry*, **15** (2023), 286. https://doi.org/10.3390/sym15020286
17. N. Anwar, M. A. Z. Raja, A. K. Kiani, I. Ahmad, M. Shoaib, C. M. Shu, Stochastic adaptive autoregressive eXogenous networks operative with Grünwald Letnikove fractional finite differences for nonlinear fractal differential system of coffee rust control model, *Int. J. Comput. Math.*, 2025, 1–42. https://doi.org/10.1080/00207160.2025.2511771
18. M. A. Z. Raja, A. Z. Abbasi, K. S. Nisar, A. Rafiq, M. Shoaib, A design of predictive intelligent networks for the analysis of fractional model of TB-virus, *Comput. Model. Eng. Sci. (CMES)*, **143** (2025). https://doi.org/10.32604/cmes.2025.058020
19. A. Fida, M. A. Z. Raja, C. Y. Chang, M. J. A. A. Raja, Z. A. Khan, M. Shoaib, Novel intelligent exogenous neuro-architecture-driven machine learning approach for nonlinear fractional breast cancer risk system, *Commun. Nonlinear Sci.*, **149** (2025), 108955. https://doi.org/10.1016/j.cnsns.2025.108955
20. I. Goodfellow, Y. Bengio, A. Courville, Y. Bengio, *Deep learning*, Cambridge: MIT press, **1** (2016).
21. Chimmula, V. K. Reddy, L. Zhang, Time series forecasting of COVID-19 transmission in Canada using LSTM networks, *Chaos Soliton. Fract.*, **135** (2020), 109864. https://doi.org/10.1016/j.chaos.2020.109864
22. F. Jiang, Y. Jiang, H. Zhi, Y. Dong, H. Li, S. Ma, et al., Artificial intelligence in healthcare: Past, present and future, *Stroke Vasc. Neurol.*, **2** (2017). https://doi.org/10.1136/svn-2017-000101
23. F. Sulayman, F. A. Abdullah, M. H. Mohd, An SVEIRE model of tuberculosis to assess the effect of an imperfect vaccine and other exogenous factors, *Mathematics*, **9** (2021), 327. https://doi.org/10.3390/math9040327
24. H. W. Hethcote, *The basic epidemiology models: Models, expressions for R0, parameter estimation, and applications*, In: Mathematical understanding of infectious disease dynamics, 2009, 1–61. https://doi.org/10.1142/7020
25. K. M. Addo, *An SEIR mathematical model for dog rabies; Case Study: Bongo District, Ghana*, PhD diss., 2012.